



HAL
open science

Uncertainty analysis for seawater intrusion in fractured coastal aquifers: Effects of fracture location, aperture, density and hydrodynamic parameters

Behshad Koohbor, Marwan Fahs, Behzad Ataie-Ashtiani, Benjamin Belfort, Craig T. Simmons, Anis Younes

► To cite this version:

Behshad Koohbor, Marwan Fahs, Behzad Ataie-Ashtiani, Benjamin Belfort, Craig T. Simmons, et al.. Uncertainty analysis for seawater intrusion in fractured coastal aquifers: Effects of fracture location, aperture, density and hydrodynamic parameters. *Journal of Hydrology*, 2019, 571, pp.159-177. 10.1016/j.jhydrol.2019.01.052 . hal-02628584

HAL Id: hal-02628584

<https://hal.inrae.fr/hal-02628584v1>

Submitted on 21 Oct 2021

HAL is a multi-disciplinary open access archive for the deposit and dissemination of scientific research documents, whether they are published or not. The documents may come from teaching and research institutions in France or abroad, or from public or private research centers.

L'archive ouverte pluridisciplinaire **HAL**, est destinée au dépôt et à la diffusion de documents scientifiques de niveau recherche, publiés ou non, émanant des établissements d'enseignement et de recherche français ou étrangers, des laboratoires publics ou privés.



Distributed under a Creative Commons Attribution - NonCommercial 4.0 International License

1 **Uncertainty analysis for seawater intrusion in fractured coastal aquifers:**
2 **Effects of fracture location, aperture, density and hydrodynamic**
3 **parameters**

4 Behshad Koohbor¹, Marwan Fahs^{1*}, Behzad Ataie-Ashtiani^{2,3}, Benjamin Belfort¹, Craig T.
5 Simmons³, Anis Younes^{1,4,5}

6
7 ¹*Laboratoire d'Hydrologie et Geochemie de Strasbourg, University of*
8 *Strasbourg/EOST/ENGEES, CNRS, 1 rue Blessig 67084 Strasbourg, France.*

9 ²*Department of Civil Engineering, Sharif University of Technology, PO Box 11155-9313,*
10 *Tehran, Iran.*

11 ³*National Centre for Groundwater Research & Training, College of Science & Engineering,*
12 *Flinders University, GPO Box 2100, Adelaide, South Australia 5001, Australia.*

13 ⁴*IRD UMR LISAH, F-92761 Montpellier, France.*

14 ⁵*Laboratoire de Modélisation en Hydraulique et Environnement, Ecole Nationale*
15 *d'Ingénieurs de Tunis, Tunisia*

16

17

18

19

20

21 Submitted to Journal of Hydrology: Special Issue “Improving model-data interaction in
22 Hydrogeology: Insights from different disciplines”.

23

24

25

26 *Contact person: Marwan Fahs

27 E-mail: fahs@unistra.fr

28

29

30 **Abstract**

31 In this study we use polynomial chaos expansion (PCE) to perform uncertainty analysis for
32 seawater intrusion (SWI) in fractured coastal aquifers (FCAs) which is simulated using the
33 coupled discrete fracture network (DFN) and variable-density flow (VDF) models. The DFN-
34 VDF model requires detailed discontinuous analysis of the fractures. In real field applications,
35 these characteristics are usually uncertain which may have a major effect on the predictive
36 capability of the model. Thus, we perform global sensitivity analysis (GSA) to provide a
37 preliminary assessment on how these uncertainties can affect the model outputs. As our
38 conceptual model, we consider fractured configurations of the Henry Problem which is
39 widely used to understand SWI processes. A finite element DFN-VDF model is developed in
40 the framework of COMSOL Multiphysics®. We examine the uncertainty of several SWI
41 metrics and salinity distribution due to the incomplete knowledge of fracture characteristics.
42 PCE is used as a surrogate model to reduce the computational burden. A new sparse PCE
43 technique is used to allow for high polynomial orders at low computational cost. The Sobol’
44 indices (SIs) are used as sensitivity measures to identify the key variables driving the model
45 outputs uncertainties. The proposed GSA methodology based on PCE and SIs is useful for
46 identifying the source of uncertainties on the model outputs with an affordable computational
47 cost and an acceptable accuracy. It shows that fracture hydraulic conductivity is the first
48 source of uncertainty on the salinity distribution. The imperfect knowledge of fracture
49 location and density affects mainly the toe position and the total flux of saltwater entering the
50 aquifer. Marginal effects based on the PCE are used to understand the effects of fracture
51 characteristics on SWI. The findings provide a technical support for monitoring, controlling
52 and preventing SWI in FCAs.

53 **Keywords:** Seawater intrusion, fractured coastal aquifers, uncertainty analysis, uncertain
54 fracture characteristics, global sensitivity analysis, Sobol’ indices

55 **1. Introduction**

56 Coastal aquifers (CAs) are currently in a critical situation throughout the world. These
57 aquifers are essential sources of freshwater for more than 40% of the world's population
58 living in coastal areas [*IOC/UNESCO, IMO, FAO, UNDP, 2011; Barragán and de Andrés,*
59 *2015*]. The phenomenon of seawater intrusion (SWI), which encompasses the advancement of
60 saline water into fresh groundwater mainly caused by excessive groundwater extraction, is the
61 first source of contamination in CAs [*Werner et al., 2013*]. The European Environment
62 Agency [*www.eea.europa.eu*] declared SWI as a major threat for many CAs worldwide. This
63 phenomenon is exacerbated by the increasing demand for groundwater as a result of the
64 increase in population and anthropogenic activity. It is also amplified due to natural causes
65 such as climate change, Tsunami events and sea-level rise expected in the next century [*e.g.,*
66 *Ataie-Ashtiani et al., 2013; Ketabchi et al., 2016*].

67 The impacts of local heterogeneities of CAs on the extent of SWI at the scale relevant for
68 management scenarios is well documented in the literature [*e.g. Simmons et al., 2001; Kerrou*
69 *and Renard, 2010; Lu et al., 2013; Mehdizadeh et al., 2014; Pool et al., 2015; Stoeckl et al.,*
70 *2015; Shi et al., 2018*]. Fractured geology is the most challenging form of natural
71 heterogeneity. Fractures represent the preferential pathways that may enable faster SWI or
72 intensify freshwater discharge to the sea [*Bear et al. 1999*]. Fractured coastal aquifers (FCAs)
73 are found globally. Several examples can be found in France [*Arfib and Charlier, 2016*],
74 USA [*Xu et al., 2018*], Greece [*Dokou and Karatzas, 2012*], Italy [*Fidelibus et al., 2011*],
75 Ireland [*Perriquet et al., 2014; Comte et al., 2018*], UK [*MacAllister et al., 2018*] and in the
76 Mediterranean zone where more than 25% of CAs are typically karstic [*Bakalowicz et al.,*
77 *2008; Chen et al., 2017*]. Despite the fact that FCAs are distributed throughout the world and
78 they often contain significant groundwater resources due to their high porosity, SWI in these
79 aquifers is rarely investigated and related processes are still largely unexplored and poorly

80 understood [Dokou and Karatzas, 2012; Sebben et al., 2015]. In the review paper of Werner
81 et al. [2013], the authors suggested SWI in FCAs as one of the potential remaining
82 challenging problems.

83 SWI can be tackled using either the sharp interface approximation or variable-density flow
84 (VDF) model [Werner et al., 2013; Llopis-Albert et al., 2016; Szymkiewicz et al., 2018]. VDF
85 model involves flow and mass transfer equations coupled by a mixture state equation
86 expressing the density in terms of salt concentration. This model is usually used in field
87 applications as it is more realistic than the sharp interface approximation and has the privilege
88 of considering the transition zone between the freshwater and saltwater, known as the mixing
89 zone. Flow in fractured porous media can be described using three alternative approaches: i)
90 equivalent porous medium in which averaged estimations of the hydrogeological properties
91 over a representative elementary volume are used to represent the domain [Dietrich et al.,
92 2005], ii) dual-porosity models where the domain is considered as the superposition of two
93 continuums representing, respectively, rocks and fractures [Fahs et al., 2014; Jerbi et al.,
94 2017] and iii) discrete fracture model in which the fractures and matrix are handled explicitly
95 [Berre et al., 2018]. Discrete fracture model is the most accurate model because fractures are
96 considered without any simplification. It is usually used for domains with a relatively small
97 number of fractures [Hirthe and Graf, 2015; Ramasomanana et al., 2018] and has come into
98 practical use in recent years. However, discrete fracture models require enormous
99 computational time and memory due to the dense meshes resulting from the explicit
100 discretization of the fractures. Discrete fracture network (DFN), in which the fractures are
101 embedded in $(d-1)$ dimensional elements in (d) dimensional physical domain, is an alternative
102 approximation that reduces the overhead computations of the discrete fracture model.

103 DFN model has been successfully coupled with VDF model to simulate SWI in FCAs. For
104 instance, Grillo et al. [2010], based on a single fracture configuration of Henry Problem,

105 showed that DFN-VDF model is a valid alternative to the discrete fracture model for
106 simulating SWI. *Dokou and Karatzas [2012]* developed a hybrid model based on the
107 combination of the DFN model (for main fractures and faults) and the equivalent porous
108 media model (for lower-order fractures) to investigate SWI in a FCA in Greece. By
109 confronting numerical simulations to chloride concentration observations, they showed that
110 the DFN model is necessary to accurately simulate SWI. *Sebben et al. [2015]* used the DFN-
111 VDF model to present a preliminary deterministic study on the effect of fractured
112 heterogeneity on SWI, using different fractured configurations of Henry Problem. *Mozafari et*
113 *al. [2018]* developed a DFN-VDF model in the finite element frame-work of COMSOL
114 Multiphysics®. Nevertheless, the DFN-VDF model requires the basic characteristics of
115 fractures as location, aperture, permeability, porosity, etc. These characteristics are subject to
116 a large amount of uncertainties as they are often determined using model calibration
117 procedure based on relatively insufficient historical data provided by several measurement
118 techniques as surface electrical resistivity tomography [*Beaujean et al., 2014*], borehole
119 concentrations and head measurements, multiperiod oscillatory hydraulic tests [*Sayler et al.,*
120 *2018*], self-potential measurements [*MacAllister et al., 2018*], among others. These
121 uncertainties would reduce the predictive capability of the DFN-VDF model and impair the
122 reliability of SWI management based on these predictions. Thus, it is important to understand
123 how these uncertainties could propagate in the model and lead to uncertainty in outputs.

124 This work goes a step further in the understanding of SWI processes in FCAs. It aims to
125 provide a preliminary investigation on the impacts of uncertainty associated to fractures
126 characteristics on the extent of the steady-state saltwater wedge simulated using the DFN-
127 VFD model. In particular, we investigate the effects of uncertainties on fracture network
128 characteristics (location, aperture, density, permeability and dispersivity) on several SWI
129 metrics, as the length of the saltwater toe, thickness of the mixing zone, area of the salted

130 zone and salinity flux penetrating to the aquifer. As the underpinning conceptual model, we
131 consider the fractured Henry Problem suggested in *Sebben et al. [2015]*. A finite element
132 DFN-VDF numerical model is implemented using COMSOL Multiphysics® software. We
133 include the Boussinesq approximation in the COMSOL model to reduce nonlinearity and
134 improve computational efficiency.

135 In order to quantify the variability in model outputs resulting from the uncertain parameters,
136 we use the global sensitivity analysis (GSA). GSA is more appropriate than local sensitivity
137 analysis as it provides a robust and practical framework to explore the entire inputs space and
138 to assess the key variables driving the model outputs uncertainty [*Saltelli, 2002; Sudret,*
139 *2008; De Rocquigny, 2012*]. GSA is a powerful approach to fully understand the complex
140 physical processes and assess the applicability of models. It is also important for risk
141 assessment and decision-making. In hydrogeological applications, GSA has been used to
142 investigate saturated/unsaturated flow [*Younes et al., 2013, 2018; Dai et al., 2017; Meng and*
143 *Li, 2017; Maina and Guadagnini, 2018; Miller et al., 2018*], solute transport [*Fajraoui et al.,*
144 *2011, 2012; Ciriello et al., 2013; Younes et al., 2016*], geological CO₂ sequestration [*Jia et*
145 *al., 2016*], natural convection [*Fajraoui et al., 2017*] and double-diffusive convection [*Shao*
146 *et al., 2017*]. In SWI, GSA has been applied to study the effects of hydrodynamics parameters
147 in homogeneous CAs [*Herckenrath et al., 2011; Rajabi and Ataie-Ashtiani, 2014; Rajabi et*
148 *al., 2015; Riva et al., 2015; Dell'Oca et al., 2017*]. *Rajabi et al. [2015]* have shown that GSA
149 is the best-suited method for uncertainty analysis of SWI. Recently, *Xu et al. [2018]* used
150 GSA to investigate SWI in a karstic CA with conduit networks. To the best of our knowledge,
151 GSA has never been applied to SWI in heterogeneous and/or FCAs. Different alternatives can
152 be used to perform GSA [*Iooss and Lemaître, 2015*]. Among these alternatives, in this paper,
153 we use the variance-based technique with the Sobol' indices (SIs) as sensitivity metrics
154 [*Sobol', 2001*]. These indices are widely used because they do not assume any simplification

155 regarding the physical model and provide the sensitivity of individual contribution from each
156 parameter uncertainty as well as the mixed contributions [*Sarkar and Witteveen, 2016*]. SIs
157 are usually evaluated through Monte Carlo methods which require a large number of
158 simulations to cover the parameters space and, as a consequence, might be impractical in high
159 CPU consuming problems (as is the case for SWI in FCAs) [*Sudret, 2008; Herckenrath et al.,*
160 *2011*]. To meet the numerical challenges of Monte Carlo methods, we use the polynomial
161 chaos expansions (PCE) which proceeds by expressing each model output as a linear
162 combination of orthogonal multivariate polynomials, for a specified probability measure
163 [*Crestaux et al., 2009; Konakli and Sudret, 2016; Fajraoui et al., 2017*]. In particular, we
164 implement the sparse PCE technique developed by *Shao et al. [2017]* to allow high
165 polynomial orders (i.e. high accuracy) with an optimized number of deterministic samples.
166 With this technique, the number of terms in the PCE decomposition is reduced by excluding
167 insignificant terms. The polynomial order is updated progressively until reaching a prescribed
168 accuracy. During the procedure, Kashyap information criterion is used to measure the
169 relevance of PCE terms [*Shao et al., 2017*]. The sparsity of the PCE allows accurate surrogate
170 model even if the optimal number of samples necessary for a total order expansion is not
171 achieved. Once the PCE is constructed for each model output, the SIs can be directly
172 calculated, with no extra computational cost, by a post-processing treatment of the PCE
173 coefficients.

174 The paper is organized as follows: Section 2 is for material and methods in which we present
175 two fractured scenarios of the Henry Problem investigated in this study, the DFN-VDF model
176 developed with COMSOL and the SWI metrics used as model outputs. Section 3 is devoted to
177 the GSA method. In section 4, we validate the developed COMSOL model and the
178 Boussinesq approximation by comparison against exact solutions and an in-house research

179 code. Section 5 discusses the GSA results; it includes PCE construction, validation of PCE
180 and uncertainties propagation. A conclusion is given in section 6.

181 **2. Material and methods**

182 *2.1. Conceptual model: Fractured Henry Problem*

183 The conceptual model is based on the fractured Henry Problem, suggested by *Sebben et al.*
184 *[2015]*. A detailed review of the Henry Problem and its applications can be found in *Fahs et*
185 *al. [2018]*. This problem deals with SWI in a confined CA of depth H and length ℓ . Sea
186 boundary condition (constant concentration and depth-dependent pressure head) is imposed at
187 the left side and constant freshwater flux ($q_d [L^2T^{-1}]$) with zero concentration is assumed at
188 the right side. Two fracture configurations are investigated in our analysis. The first
189 configuration deals with a single horizontal fracture (SHF) extending on the whole domain
190 and located at a distance (d^F) from the aquifer top surface (Fig. 1a). This configuration is
191 specifically considered to investigate the effect of uncertainty related to fracture location on
192 the extent of saltwater wedge. In the second configuration, we assume a network of
193 orthogonal fractures (NOF) (Fig. 1b), as in *Sebben et al. [2015]*. Square sugar-cube model
194 with elementary size δ^F (distance between 2 consecutive fractures) is considered as fracture
195 network. This configuration is considered since it allows for performing uncertainty analysis
196 of the SWI metrics with respect to the fracture density. Furthermore, vertical fractures are
197 important to investigate buoyancy effects.

198 *2.2. DFN-VDF mathematical model:*

199 Under steady-state conditions and based on Boussinesq approximation, the VDF model in the
200 porous matrix is given by *[Guevara Morel et al., 2015]*:

$$\nabla \cdot \mathbf{q} = 0 \tag{1}$$

$$\mathbf{q} = -K^M \left(\nabla h + \frac{\rho - \rho_0}{\rho_0} \nabla z \right) \quad (2)$$

$$\mathbf{q} \nabla c - \nabla \cdot (\varepsilon^M D_m \mathbf{I} + \mathbf{D}) \nabla c = 0 \quad (3)$$

$$\mathbf{D} = (\alpha_L^M - \alpha_T^M) \frac{\mathbf{q} \times \mathbf{q}}{|\mathbf{q}|} + \alpha_T^M |\mathbf{q}| \mathbf{I} \quad (4)$$

$$\rho = \rho_0 + \Delta \rho c \quad (5)$$

201 where q is the Darcy's velocity [LT^{-1}]; ρ_0 the freshwater density [ML^{-3}]; g the gravitational
 202 acceleration [LT^{-2}]; K^M is the freshwater hydraulic conductivity of the porous matrix
 203 [LT^{-1}]; h the equivalent freshwater head [L]; ρ [ML^{-3}] the density of mixture fluid and z
 204 is the elevation [L]; c is the relative solute concentration [-]; D_m the molecular diffusion
 205 coefficient [L^2T^{-1}]; ε^M is the porosity [-] of the porous matrix; \mathbf{I} the identity matrix and \mathbf{D}
 206 is the dispersion tensor; α_L^M [L] and α_T^M [L] are the longitudinal and transverse dispersion
 207 coefficient of the porous matrix, respectively.

208 With the DFN approach, the mathematical model for fractures can be obtained by assuming
 209 1D flow and mass transport equations along the fractures direction. The resulting equations
 210 are similar to the ones in the porous matrix, but with ε^F , K^F and α_L^F as porosity, hydraulic
 211 conductivity and longitudinal dispersivity in the fractures, respectively. Transverse
 212 dispersivity in the fracture (α_T^F) is neglected, as in *Sebben et al. [2015]*. The 1D flow and
 213 mass transport equations in fracture involve the thickness of the fracture (e^F) as parameter.

214 2.3. DFN-VDF finite element model: COMSOL Multiphysics®:

215 The DFN-VDF simulations are performed using a finite element model developed with
 216 COMSOL Multiphysics® software package. COMSOL is a comprehensive simulation

217 software environment for various applications. The use of COMSOL in applications related to
218 hydrogeology is increasingly frequent as this software is a user-friendly tool that facilitates all
219 the modeling steps (preprocessing, meshing, solving and post-processing) and allows an easy
220 coupling of different physical processes [Ren et al., 2017; Fischer et al., 2018]. Our
221 COMSOL model is created by coupling the “Subsurface Flow” and “Transport of Diluted
222 Species” modules and by assuming concentration-dependent fluid density. The Subsurface
223 Flow module is an extension of COMSOL modeling environment to applications related to
224 fluid flow in saturated and variably saturated porous media. In this module, we use the
225 “Darcy’s Flow” interface. The fractures are included via the DFN model by adding the
226 “Fracture Flow” feature to the “Darcy's law” interface. The “Transport of Diluted Species”
227 module is used to solve the advection-dispersion equation. The Boussinesq approximation is
228 implemented by considering constant density in the fluid properties and setting a buoyancy
229 volume force depending on the salt concentration. The numerical scheme suggested by
230 default in COMSOL is used to solve the system of equations. The flow and transport models
231 are solved sequentially via the segregated solver. Accurate solutions of the flow model can be
232 obtained using finite volume or finite difference methods [Deng and Wang, 2017]. However,
233 in COMSOL, quadratic basis finite element functions are used for the discretization of the
234 pressure in the flow model while the concentration in the transport model is discretized using
235 the linear basis functions. The consistent stabilization technique is used to avoid unphysical
236 oscillations related to the discretization of the advection term. This technique is often called
237 upwinding. It adds diffusion in the streamline direction. Triangular meshes suggested by the
238 COMSOL meshing tool are used in the simulations. With the DFN model, the COMSOL
239 meshing tool generates 2D triangular cells to represent the matrix and 1D cells to represent
240 the fractures. The fracture cells are positioned along the sides of the matrix triangular cells.
241 With the finite-element modeling framework, the common degrees of freedom at the triangle

242 nodes in the matrix and at the 1D segments in the fractures are used to model the volumetric
243 and mass fluxes between the matrix and the fractures. First runs have shown that, with the
244 steady-state mode, COMSOL is bound to run into convergence difficulties. To avoid this
245 problem, we used the transient mode. This problem is related to the initial guesses, required
246 for the nonlinear solver, that are often hard to obtain. Hence, the steady-state solutions are
247 obtained by letting the system evolve under transient conditions until steady-state.

248 *2.4. Metrics Design:*

249 The main purpose of this study is to perform GSA in regards to certain metrics characterizing
250 the steady state salt-wedge and saltwater flux associated with SWI. The model inputs will be
251 discussed later in the results section since they are dependent on the fracture configuration. As
252 model outputs, we consider the following SWI metrics:

- 253 - The spatial distribution of the salt concentration: It is obtained in a pattern of a
254 100×50 regular 2D square grid (5,000 nodes).
- 255 - Length of the saltwater toe (L_{toe}): The distance from sea boundary to the 0.5
256 isochlor on the bottom surface of the aquifer (Fig. 2).
- 257 - Thickness of the saltwater wedge (L_S): The distance between the 0.1 and 0.9
258 isochlors on the aquifer bottom surface (Fig. 2).
- 259 - Average horizontal width of the mixing zone (\bar{W}_{mz}): The average horizontal
260 distance between the 0.1 and 0.9 isochlors from the bottom to the top of the
261 aquifer (Fig. 2).
- 262 - The height of the inflection point (Z_I): The freshwater-seawater inflection point
263 located on the seaward boundary (Fig. 2). Below this point, the seawater flows
264 toward the land, and above it the freshwater is discharged to the sea.

265 - The dimensionless mass of salt persisting in the aquifer $\left(M_s = \frac{1}{\ell.H} \int_0^\ell \int_0^H c.xdz \right)$:

266 The double integral is calculated with the grid used for the spatial distribution of
267 salt concentration. Only nodes with concentration above 0.01 are considered.

268 - Total dimensionless flux of saltwater entering the aquifer (Q_s^{total}): defined as the
269 flux of saltwater entering the domain by advection, diffusion and dispersion
270 normalized by the freshwater flux imposed at the inland boundary (q_d).

271 3. Global sensitivity analysis

272 GSA is a useful and a widespread tool that aims to quantify and evaluate the output
273 uncertainties resulting from the uncertainties in the model inputs, which could be considered
274 singly (for one parameter) or coupled together (several parameters). In this study, the
275 variability of the model responses is quantified throughout a variance based technique using
276 SIs as sensitivity metrics. On the one hand, variance-based sensitivity measures are of interest
277 as they typically specify the relationship between model outputs and input parameters. And on
278 the other hand, the major advantage of using SIs is that they do not require any assumptions
279 of monotonicity or linearity in the physical model. The main stages of this technique are
280 developed here. More details can be found in *Sudret [2008]*, *Fajraoui et al. [2017]* and *Le*
281 *Gratiet et al. [2017]*

282 Let us consider a mathematical model, $Y = M(\mathbf{X})$, delivering the outputs of a physical
283 system that presumably depends on M-uncertain input parameters $\mathbf{X} = \{X_1, X_2, \dots, X_M\}$. For
284 further developments, $f_{X_i}(x_i)$ and $f_x = \prod_{i=1}^M f_{X_i}(x_i)$ refer to their marginal probability
285 density function (PDF) and the corresponding joint PDF of a given set.

286 3.1 Sobol' indices

287 The Sobol' decomposition of $M(\mathbf{X})$ reads [Sudret, 2008; Fajraoui et al., 2017]:

$$M(\mathbf{X}) = M_0 + \sum_{i=1}^M M_i(X_i) + \sum_{1 \leq i < j \leq M} M_{ij}(X_i, X_j) + \dots + M_{1,2,\dots,M}(X_1, \dots, X_M), \quad (6)$$

288 where M_0 is the expected value of $M(\mathbf{X})$ and the integral of each summand

289 $M_{i_1, i_2, \dots, i_s}(X_{i_1}, X_{i_2}, \dots, X_{i_s})$ over any of its independent variables is zero, that is:

$$\int_{\Gamma_{X_{i_k}}} M_{i_1, i_2, \dots, i_s}(X_{i_1}, X_{i_2}, \dots, X_{i_s}) f_{X_{i_k}}(x_{i_k}) = 0 \text{ for } 1 \leq k \leq s, \quad (7)$$

290 where $f_{X_{i_k}}(x_{i_k})$ and $\Gamma_{X_{i_k}}$ represent the marginal PDF and support of X_{i_k} , respectively.

291 The orthogonality M_i leads a unique Sobol' decomposition:

$$E[M_u(X_u)M_v(X_v)] = 0, \quad (8)$$

292 Where, $E[\cdot]$ is the mathematical expectation operator, $u = \{i_1, i_2, \dots, i_M\} \subseteq \{1, 2, \dots, M\}$

293 represents the index sets and X_u are the subvectors involving the components for which the

294 indices belong to u . As a result of uniqueness and orthogonality of Y , its total variance D is

295 decomposed as below:

$$D = \text{Var}[\mathcal{M}(X)] = \sum_{u \neq 0} D_u = \sum_{u \neq 0} \text{Var}[\mathcal{M}_u(X_u)], \quad (9)$$

296 where D_u is the partial variance expressed as below:

$$D_u = \text{Var}[\mathcal{M}_u(X_u)] = E[\mathcal{M}_u^2(X_u)] \quad (10)$$

297 Consequently, the SIs are naturally defined as:

$$S_u = \frac{D_u}{D} \quad (11)$$

298 The influence on Y , of each parameter (considered singly), is given by the first order Sobol'

299 indices (S_i) defined by:

$$S_i = \frac{D_i}{D} \quad (12)$$

300 The total SI that includes the effect of an input parameter with the contribution from other
 301 parameters, is defined as follows [Homma and Saltelli, 1996]:

$$S_i^T = \sum_{\vartheta_i} \frac{D_u}{D}, \quad \vartheta_i = \{u \supset i\} \quad (13)$$

302 The SIs can be calculated by performing Monte-Carlo simulations. This can be done using the
 303 estimates of the mean value, total and partial variance of a large number of samples, as
 304 explained in Sudret [2008]. The drawback of Monte-Carlo simulations lies in the
 305 computational cost especially when time-consuming models are investigated. To circumvent
 306 this problem, Sudret [2008] introduced the PCE for the computation of SIs.

307 3.2 Polynomials chaos expansion (PCE)

308 Each model output is expanded into a set of orthonormal multivariate polynomials of
 309 maximum degree M:

$$Y = M(X) \approx \sum_{\alpha \in A} y_\alpha \Phi_\alpha(X), \quad (14)$$

310 where A is a multi-index $\alpha = \{\alpha_1, \alpha_2, \dots, \alpha_M\}$ and $\{y_\alpha, \alpha \in A\}$ are the polynomial coefficients.

311 $\Phi_\alpha(X)$ are the base functions of vector space of polynomial functions. These functions
 312 should be orthogonal in the vector space with the joint PDF f_X of X as a dot product.

313 The polynomial coefficients $\{y_\alpha\}$ are evaluated using the regression method (least-square
 314 technique) that proceeds by minimizing an objective function representing the difference
 315 between the meta-model and physical model (see Fajraoui et al. [2017]). Based on the PCE,
 316 the mean value (μ) and total variance (D) of any model output can be calculated as follows:

$$\mu = y_0 \quad (15)$$

$$D = \sum_{\alpha \in A \setminus \{0\}} y_\alpha^2 \quad (16)$$

317 Then the SIs of any order can be computed using the coefficients, D and μ in a
 318 straightforward manner as followed:

$$S_i = \sum_{\alpha \in A_i \setminus \{0\}} y_\alpha^2 / D, \quad A_i = \{\alpha \in A : \alpha_i > 0, \alpha_{j \neq i} = 0\}, \quad (17)$$

319 and

$$S_i^T = \sum_{\alpha \in A_i^T \setminus \{0\}} y_\alpha^2 / D, \quad A_i^T = \{\alpha \in A : \alpha_i > 0\} \quad (18)$$

320 As suggested by *Deman et al. [2016]*, we also evaluate the marginal effect (ME) to
 321 understand the relation between the important variables and the model outputs. ME is given
 322 by:

$$E[\mathcal{M}(X) | X_i = x_i] = \mathcal{M}_0 + \sum_{\alpha \in A_i} y_\alpha \Phi_\alpha(x_i) \quad (19)$$

323 3.3 Sparse polynomial chaos expansion

324 To minimize the number of physical model evaluations and therefore reduce the
 325 computational cost, the estimation of the Sobol' indices could be done with a sparse PCE
 326 instead of a full PCE approach. In other words, instead of using the expression Eq. (14), we
 327 can only use some relevant coefficients of the PCE. The key idea consists in discarding the
 328 irrelevant terms in the estimated truncated PCE and for this purpose, several approaches have
 329 been developed. *Blatman and Sudret [2010]* utilized an iterative forward–backward approach
 330 based on nonintrusive regression or a truncation strategy based on hyperbolic index sets
 331 coupled with an adaptive algorithm involving a least angle regression (LAR). *Meng and Li*
 332 *[2017]* modified the LAR algorithm with a least absolute shrinkage and selection operator
 333 (LASSO-LAR). An adaptive procedure using projections on a minimized number of bivariate
 334 basis functions has been provided by *Hu and Youn [2011]*, whereas *Fajraoui et al. [2012]*
 335 worked with a fixed experimental design and retained only significant coefficients that could

336 contribute to the model variance. The approach developed in *Shao et al. [2017]*, which has
337 been implemented in this work, consists in progressively increasing the degree of an initial
338 PCE until a satisfactory representation of the model responses is obtained. The computation
339 of the Kashyap information criterion (KIC) based on a Bayesian model averaging is used to
340 determine the best sparse PCE for a input/output sample. Evaluating KIC is an efficient (from
341 a computational point of view) and feasible alternative to directly computing the Bayesian
342 model evidence, being known that this later evaluates the likelihood of the observed data
343 integrated over each model's parameter space. Hence, it is a key term to obtain the posterior
344 probability in the Bayesian framework. For more details on the Bayesian sparse PCE, for
345 constructing the algorithm and computing the KIC, readers can refer to *Shao et al. [2017]*.

346 **4. Validations: COMSOL model and Boussinesq approximation**

347 Although COMSOL has great potential for modelling density-driven flow problems, it has
348 rarely been used for SWI. Thus, the main purpose of this section is to validate our developed
349 COMSOL model. In addition, as explained previously, Boussinesq approximation was
350 implemented in our COMSOL model to improve its computational efficiency. This is a
351 popular approximation for the VDF model as it allows for reducing the computational costs
352 and renders convergence more likely to be achieved. It assumes that variations in density only
353 give rise to buoyancy forces and have no impact on the flow field. Boussinesq approximation
354 ignores density-concentration dependence except in the buoyancy term. This approximation is
355 common for SWI in non-fractured CAs [*Guevara Morel et al., 2015*]. Its validity for SWI in
356 FCAs is not discussed in the literature. Thus, another goal of this section is to investigate the
357 validity of this approximation for such a case.

358 For this purpose, we first use the new semi-analytical solutions of the Henry Problem
359 (homogeneous aquifer) developed by *Fahs et al. [2016]*. We compare these solutions against

360 two COMSOL models: i) SWI-COMSOL model based on the standard COMSOL approach
361 and ii) SWI-COMSOL-Bq based on the Boussinesq approximation. We investigate two test
362 cases presented in *Fahs et al. [2016]* which deal with constant and velocity-dependent
363 dispersion tensor, respectively. The corresponding physical parameters are summarized in
364 Table 1. It is noteworthy that, for the validation cases, similar to the semi-analytical solution,
365 the sea boundary is assumed at the right side of the domain. The main isochlors (0.1, 0.5 and
366 0.9) obtained with COMSOL models as well as the semi-analytical ones are plotted in Fig. 3.
367 The corresponding SWI metrics are given in Table 2. The COMSOL simulations have been
368 performed using a mesh consisting of about 18,000 elements. As is obvious from Fig. 3,
369 excellent agreement is obtained between the COMSOL and the semi-analytical results. This
370 highlights the accuracy of the developed COMSOL models and the related post-treatment
371 procedure applied to obtain the SWI metrics. It also confirms the validity of the Boussinesq
372 approximation for SWI in homogenous CAs.

373 For FCAs, analytical or semi-analytical solutions do not exist. We compare the developed
374 COMSOL models (SWI-COMSOL and SWI-COMSOL-Bq) against an in-house research
375 code (TRACES) based on advanced space and time discretization techniques [*Younes et al.,*
376 *2009*]. This code has been validated by comparison against several configurations of semi-
377 analytical solutions in *Fahs et al. [2018]*. It has proven to be a robust tool for the simulation
378 of SWI in both homogeneous and heterogeneous domains. DFN approach, which is based on
379 average properties over the fracture width, is not available in TRACES. Thus, the fractures
380 are modeled by considering heterogeneity of material without reduction of the dimensionality;
381 i.e. fracture is a specific layer of the 2D domain with different assigned properties. We
382 considered two validation cases which are based on a single horizontal and vertical fractures,
383 respectively. The horizontal fracture is located at the aquifer middle-depth ($d^F = 0.5m$)
384 while the vertical fracture is located near the seaside at $x=1.8m$. The physical parameters are

385 given in Table 1. The mesh used in the COMSOL simulations involves about 50,000
386 elements. In the in-house code we use a mesh with about 70,000 elements. The obtained main
387 isochlors are given in Fig. 4 and the corresponding SWI metrics are summarized in Table 2.
388 Fig. 4a shows that, in the case of single horizontal fracture, the high conductivity in the
389 fracture increases the freshwater discharge to the sea and pushes the saltwater wedge toward
390 the sea, especially around the fracture. In the case of vertical fracture (Fig. 4b), the high
391 permeability in the fracture enhances the upward flow and push up the saltwater around the
392 fracture Fig. 4 and Table 2 show excellent agreement between COMSOL and TRACES. They
393 confirm the validity of the Boussinesq approximation in the presence of fractures and
394 highlight the accuracy of the developed COMSOL model. It should be noted also that the
395 comparison between the COMSOL model (in which the fracture is considered as a line) and
396 TRACES (in which the fracture is a 2D layer) confirms the results of *Grillo et al. [2010]*
397 about the validity of the technique based on $(n-1)$ dimensional fractures (i.e. average
398 properties over the fracture) for the simulation of SWI in FCAs.

399 **5. Global sensitivity Analysis: results and discussion**

400 The methodology used to perform GSA is described in the flowchart presented in Fig. 5. In
401 this section we present the assumptions and numerical details related to the PCE construction.
402 We also validate the PCE meta-model by comparison against physical COMSOL model and
403 we present the results of the GSA based on the SI's, for both salinity distribution and SWI
404 metrics.

405

406

407 *5.1 The single horizontal fracture configuration (SHF)*

408 Several studies showed that, under steady-state condition, the isotropic Henry Problem is
409 governed by six dimensionless quantities which are the gravity number, longitudinal and
410 transverse Peclet numbers, ratio of the fresh water density to the difference between
411 freshwater and saltwater densities, Froude number and the concentration of salt in seawater
412 [Riva et al., 2015; Fahs et al., 2018]. Uncertainty analysis related to these parameters is
413 performed in Riva et al. [2015]. The main goal of our work is to investigate the effect of
414 uncertainties related to the presence of fractures. Thus, for the SHF configuration, we assume
415 that the hydraulic conductivity (K^F), aperture (e^F), depth (d^F) and longitudinal dispersivity
416 (α_L^M) of the fracture are uncertain. For the matrix domain, we only include the longitudinal
417 dispersivity (α_j^M) in our analysis as this parameter is important for the exchange between
418 fracture and matrix domain. The dispersivity ratio (transverse to longitudinal) is set to be 0.1.
419 Other parameters are kept constant. Table 3 summarizes the values of the deterministic
420 parameters as well as the range of variability of the uncertain parameters. The values used in
421 this table are similar to Sebben et al. [2015].

422 We should mention that network connectivity (i.e. how fractures are interconnected) has a
423 clear and large impact on the extent of SWI. However, in the cases investigated in this work,
424 all the fractures are fully connected (abutting and crossing fractures). Thus the effect of
425 network connectivity is not considered. Disconnected cases are not considered because it is
426 not obvious to find well defined parameters (required for GSA) to describe the connectivity.
427 Also, disconnected fractures can lead to discontinuous model outputs for which the PCE
428 surrogate model could not approximate the true system with an acceptable degree of accuracy.

429

430

431 - PCE construction: Numerical details, orders and accuracy

432 The uncertain parameters are assumed to be uniformly distributed over their ranges of
433 variability. The PCEs are evaluated using an experimental design consisting of 100 samples.
434 To obtain a deterministic experimental design that covers the parameter space, we use the
435 Quasi-Monte-Carlo sampling technique. A preliminary mesh sensitivity analysis is performed
436 to ensure mesh-independent solutions for all the simulated samples. These simulations were
437 important in order to verify that the GSA results are not affected by numerical artifacts related
438 to the finite element discretization. The mesh sensitivity analysis is performed using the most
439 challenging numerical case that deals with the highest value of K^F and lowest values of α_L^M
440 , α_L^F and e^F . In such a case the advection and buoyancy processes are very important and the
441 corresponding numerical solution could be highly sensitive to the mesh size as it might suffer
442 from unphysical oscillations or numerical diffusion. A mesh-independent solution is achieved
443 for this case using a grid consisting of about 50,000 elements. This mesh is used for the 100
444 simulations required for computing the PCE expansions.

445 For each SWI metric (or model output), the corresponding PCE surrogate model is calculated
446 using the technique described in section 3. For the salt concentration distribution (multivariate
447 output), component-wise PCE is constructed on each node of the regular 2D square grid
448 defined for the control points (involving 5,000 control points). The MATLAB code developed
449 by *Shao et al. [2017]* is used to compute the sparse PCE. To give more confidence to the
450 sparse PCE, we also compute total order PCE using the UQLAB software [*Marelli and*
451 *Sudret, 2014*]. As five input variables are considered and 100 samples are available, only
452 third-order polynomial could be reached via the total order PCE expansion. The
453 corresponding optimal number of samples is 56. With the sparse technique, implemented in
454 this work, higher orders can be reached even if the optimal number of samples required for
455 full PCE is not achieved. Sixth order PCE is reached for the salt concentration distribution
456 and all SWI metrics except the width of the mixing zone for which the polynomial order is

457 limited to five. The accuracy of the resulting sparse PCE surrogate model is checked by
458 comparison against the physical COMSOL model. In Fig. 6, we compare the values obtained
459 with the sparse PCE with those of DFN-VDF physical model implemented with COMSOL
460 for parameter inputs corresponding to the experimental design (i.e. used for the PCE
461 construction) and also for new samples. Some examples of the results, precisely the length of
462 saltwater toe (L_{toe}) and the mass of salt persisting in the aquifer (Ms), are plotted in Fig. 6.
463 We can observe an excellent match which confirms that the PCE surrogate model reproduces
464 the physical model outputs well.

465 *- Uncertainty propagation and Marginal Effects (ME)*

466 Based on the PCE, we calculate the first and total SIs which are used for uncertainty
467 propagation. We also calculate the ME (univariate effect) to obtain a global idea about the
468 impact of the input parameters on the model output. The ME of a certain parameter represents
469 the variability of the model output to this parameter when other parameters are kept constant,
470 at their average values.

471 The GSA results for the spatial distribution of the salt concentration are illustrated in Fig. 7.
472 Fig. 7a shows the distribution of the mean concentration based on the PCE expansion. At each
473 node of the mesh used for the control points, the mean value of the salt concentration is
474 calculated as the arithmetic average of the concentrations corresponding to the 100 samples
475 used in the experimental design which are evaluated via the PCE surrogate model. This figure
476 shows that the mean concentration distribution reflects the systematic behavior of SWI. The
477 isochlors are more penetrated at the bottom aquifer due to the saltwater density. This confirms
478 that the PCE surrogate model mimics the full model's response. We also calculate the
479 concentration variance to evaluate how far the concentrations are spread out from their
480 average values (Fig. 7b). As expected, the variance is significant in the saltwater wedge. The

481 largest values are located near the aquifer bottom surface where the SWI is usually induced by
482 mixing processes that can be highly sensitive to the model inputs (fracture characteristics and
483 matrix dispersivity). The variance is negligible near the sea-side as the boundary conditions
484 are almost deterministic and the sole acting random parameter is the longitudinal dispersivity
485 that can affect the dispersive entering flux. The sensitivity of the concentration distribution to
486 the uncertain parameters is assessed with the maps of the total SI (Figs 7 c-g). The total SI of
487 α_L^M (Fig. 7c) shows that the uncertainty related to this parameter affects the concentration
488 distribution at the top aquifer, outside the saltwater wedge. In this zone, the salt transport
489 processes are dominated by the longitudinal dispersion flux as the velocity is toward the sea
490 and it is almost horizontal and parallel to the salt concentration gradient. The zones of largest
491 total SI for K^F and e^F are located within the saltwater wedge toward the low isochlors (Fig.
492 7d and 7e). In this region, the mass transfer is mainly related to the advection process which is
493 related to the velocity field. This later is highly depending on the fracture permeability and
494 aperture. The zone of influence of d^F is also located within the saltwater wedge, but toward
495 the aquifer bottom surface and at the vicinity of the high isochlors (Fig. 7f). The influence of
496 α_L^F is limited to the vicinity of the sea boundary where α_L^F can impact the saltwater flux to
497 the aquifer (Fig. 7g). In the fracture, advection is dominating and dispersion is negligible. It is
498 worthwhile noting that the total SIs count in the overall contribution of a parameter including
499 nonlinearities and interactions. Thus, SIs allow for ranking the parameters according to their
500 importance. It appears on Figs. 7 that d^F , K^F and e^F are the most influential parameters
501 because their total SI are more pronounced in the region where the salt concentration variance
502 is maximum. From the scales of Figs. 7 (d-f), it is clear that K^F and e^F are more influential
503 than d^F . Figs. 7c shows that the salinity distribution is weakly sensitive to the longitudinal
504 dispersivity of the matrix as in its zone of influence the variance is negligible.

505 Inspection of the sensitivity of SWI metrics to uncertain parameters is given in Fig. 8. This
 506 figure represents the bar-plots of the total and first-order SIs of the SWI metrics. As
 507 mentioned previously for a further understanding of the uncertainty on SWI metrics related to
 508 the imperfect knowledge of input parameters, we also investigate the MEs of the most
 509 relevant parameters. These MEs are plotted in Fig. 9. The large variability of the SWI metrics
 510 (see vertical scales in Figs. 9a-j) confirms that the MEs are in agreement with the SIs.

511 Fig. 8a shows that the uncertainty on L_{toe} is mainly due to the effects of d^F and K^F . With a
 512 total SI of 0.54, d^F is considered as the most influential parameter. The ME of d^F and K^F on
 513 L_{toe} are given in Fig. 9a and 9b, respectively. Fig. 9a shows that L_{toe} decreases with d^F
 514 which is coherent with the results of *Sebben et al. [2015]*. Fig. 9b shows that L_{toe} increases
 515 with K^F . The physical interpretation of this variation is that the increase of K^F heightens the
 516 potential of the fracture to constitute a preferential freshwater flow path. This slow down the
 517 freshwater flow in the matrix which in turn facilitates SWI and leads to the increase of the
 518 penetration length of the saltwater wedge. Fig. 8b indicates that the variability of L_S is mainly
 519 impacted by α_L^M . This makes sense as L_S measures the salinity dispersion along the aquifer
 520 bottom surface which is mainly controlled by α_L^M . L_S is even expected to increase with α_L^M ,
 521 which is confirmed from the ME in Fig. 9c. We can also notice in Fig. 8b the slight sensitivity
 522 of L_S to d^F . The corresponding ME (Fig. 9d) shows that this sensitivity is relatively
 523 important for deep fractures ($d^F > 0.6$).

524 The SIs for \overline{W}_{mz} are given in Fig. 8c. The width of the mixing zone is mainly controlled by
 525 the dispersive flux. This is why, α_L^M is the main parameter affecting \overline{W}_{mz} . As expected,
 526 increasing variation of \overline{W}_{mz} against α_L^M can be observed in Fig. 9e. For Z_I (Fig. 8d), with a

527 total SI of 0.58, d^F is the most important parameter. Fig. 9f shows that Z_I decreases with d^F ,
528 which is in agreement with the results of *Sebben et al. [2015]*. Variability of Z_I could be also
529 affected by the uncertainty of K^F . The corresponding ME in Fig. 9g shows that Z_I increases
530 with K^F . Fig. 8e depicts the SIs for the mass of salt persisting in the aquifer (M_S). It indicates
531 that M_S is primarily sensitive to d^F (SI=0.62). It is also sensitive to K^F . ME (Fig. 9h) shows
532 that M_S decreases with d^F , which is also consistent with the results *Sebben et al. [2015]*.
533 M_S increases with K^F (Fig. 9i). This behavior is related to fact that the increase of K^F
534 enhances the inland extent of the saltwater wedge, as explained in the previous section.
535 Finally, the SIs for Q_S^{total} shows that this output is mainly affected by d^F (Fig. 8f). As show
536 in Fig. 9j (Q_S^{total}) increases with d^F . In general, the SIs show that the uncertainty associated
537 with α_L^F has no effect on the SWI metrics, which is logical, as salt transport in the fracture is
538 dominated by the advection processes.

539 5.2 The network of orthogonal fractures configuration (NOF)

540 In this configuration, our goal is to investigate the effect of uncertainty related to the fractures
541 density on the model outputs. Thus, we keep the same uncertain parameters as for the SHF
542 configuration but we replace (d^F) by (δ^F). The latter is considered here as the parameter
543 representing the fracture density. The values of the deterministic parameters and the range of
544 variability of the uncertain inputs are given in Table 3. The lowest value of δ^F corresponds to
545 a network with 13 horizontal and 26 vertical fractures. These values are used to obtain the
546 results in affordable CPU time, as denser fractured configurations would require a large
547 number of simulations to construct the PCE and the COMSOL model in this case becomes
548 very CPU time consuming. We should mention that, for this configuration, we reduce the

549 hydraulic conductivity of the fractures. If the same values would have been used as in SHF
550 configuration, freshwater flow would have been so intensive that no SWI would occur.

551 *- PCE construction: Numerical details, orders and accuracy*

552 The NOF configuration is more sensitive to the fractures characteristics than SHF
553 configuration. The number of samples is progressively increased until obtaining accurate
554 PCEs. The corresponding experimental design involves 200 samples. The mesh sensitivity
555 analysis for the most challenging cases (the smallest value of δ^F) reveals that mesh-
556 independent solution can be obtained using a grid of 70,000 elements. As for the SHF
557 configuration, sparse and total PCE are calculated. With 200 samples, order 4 total PCE can
558 be obtained. The optimal number of samples is 126. With the sparse technique, sixth order
559 polynomial is reached for L_{toe} , M_S , Z_I and Q_S^{total} . For L_S and \bar{W}_{mz} orders 4 and 8 are
560 achieved, respectively. Fig.10 shows some comparisons between the sparse PCE surrogate
561 and COMSOL models and highlights the accuracy of the PCE expansions. A good matching
562 is observed both for the input parameters of the experimental design and for new samples. It
563 is relevant to emphasize that this level of accuracy is acceptable to obtain good GSA results
564 with the SIs evaluated using the surrogate model.

565 *- Uncertainty propagation and marginal effects*

566 The distribution of the mean concentration based on the PCE expansion is given in Fig. 11a.
567 The mean PCE isochlors emulate the ones obtained using the physical model (Fig. 12). They
568 present some discontinuous points where saltwater is pushed toward the sea due to high
569 permeability in the fractures. The spatial map of the concentration variance is plotted in Fig.
570 11b. Compared to the SHF configuration, the zone of significant variance is contracted and
571 concentrated toward the bottom surface of the aquifer near the low mean isochlors. The map
572 of the total SIs of α_L^M (Fig. 11.c) is quite similar to the one in the SHF configuration but it

573 echoes the presence and influence of fracture network. Fig.11c shows that the zone of
574 influence of α_L^M falls where the concentration variance is negligible. Thus, α_L^M is not an
575 important parameter for salinity distribution. Sensitivity to K^F and e^F are both important
576 (Fig. 11d and e). The zone of influence of K^F is discontinuous and mainly located toward
577 the sea boundary in at the bottom of the aquifer. Important values can be observed landward
578 (see Fig. 11. d) but these values do not express high sensitivity as the concentration variance
579 is negligible in this zone. The sensitivity to the fractures density (δ^F) is given in Fig. 11f.
580 This figure shows that uncertainty associated δ^F can mainly affect the salinity distribution
581 within the mixing zone toward the bottom surface. It confirms that δ^F is an influential
582 parameter. Finally, and in contrast to the SHF configuration, α_L^F appears to be an important
583 parameter in the NOF configuration (Fig. 11g). It affects mainly salinity distribution around
584 the low isochlors.

585 The bar-plots in Fig. 13 depict the total and first-order SIs for the SWI metrics to the
586 uncertain parameters and Fig. 14 gives the MEs of these parameters. In general Fig. 14
587 confirms the results of the SIs as large variations of SWI metrics can be observed with respect
588 to the uncertain parameters. Fig. 13a demonstrates that L_{toe} is mainly controlled by K^F and
589 δ^F . The corresponding total SIs are $S_{K^F}^T = 0.52$ and $S_{\delta^F}^T = 0.32$, respectively. Fig. 14a shows
590 an increasing variation of L_{toe} against K^F . As for the SHF configuration, this is related to the
591 fact that the increase of K^F concentrates the freshwater flow in the fractures and entails a
592 weaker freshwater flow in the matrix. As consequence, the saltwater wedge expands landward
593 and L_{toe} increases. This behavior can be understood also using the equivalent porous media
594 model which is based on a bulk hydraulic conductivity. As given in *Sebben et al. [2015]*, the
595 bulk equivalent conductivity (K^{eq}) for a network of orthogonal fractures is given by:

$$K^{eq} = \left[\left(K^M + \frac{K^F e^F}{\delta^F} \right)^{-1} + \frac{e^F}{K^F \delta^F} \right]^{-1} \quad (20)$$

596 Eq. (20) shows that K^{eq} increases with the increase of K^F . The equivalent gravity number,
 597 which compares the buoyancy forces to the inland freshwater flux, is given by [Fahs et al.
 598 2018]:

$$Ng^{eq} = \frac{K^{eq} \cdot H \cdot (\rho_1 - \rho_0)}{\rho_0 q_d} \quad (21)$$

599 The increase of K^{eq} leads to the increase of Ng^{eq} . This latter can be interpreted, at constant
 600 densities and hydraulic conductivity, as a decrease in the inland freshwater that opposes SWI.
 601 This enhances the extend of SWI and leads to the increase of L_{toe} .

602 Fig. 14b shows that L_{toe} decreases with δ^F . In fact, the increase of δ^F corresponds to the
 603 reduction of the fracture density. This enhances the freshwater flow in the porous matrix and
 604 pushes the saltwater wedge toward the sea. The equivalent bulk hydraulic conductivity model
 605 can be also useful in explaining this variation, by reasoning in the same way as for the
 606 variation of L_{toe} against K^F . As it is clear from Eq. (20), the increase of δ^F (for the average
 607 value of K^M , K^F and e^F) corresponds to a decrease in K^{eq} and the related equivalent gravity
 608 number. This can be interpreted as an increase of the freshwater flux that lowers the extent of
 609 SWI and decreases L_{toe} .

610 The bar-plots in Figs. 13b and 13c indicate that, as for the SHF configuration, α_L^M is the most
 611 important parameter affecting L_S and \bar{w}_{mz} . The corresponding SIs are calculated to be 0.68
 612 and 0.34, respectively. Figs. 14c and 14d display increasing variation of L_S and \bar{w}_{mz} against
 613 α_L^M . This makes sense as L_S and \bar{w}_{mz} are mainly related to the mixing processes which are
 614 controlled by α_L^M . Fig. 13d shows that, with $S_{K^F}^T = 0.50$ and $S_{\delta^F}^T = 0.27$, K^F and δ^F are the

615 most important parameters affecting Z_I . MEs in Figs. 14e and 14f indicate that Z_I increases
 616 with K^F and decreases with δ^F . The reason behind these variations is the enhancement (resp.
 617 reduction) in the saltwater wedge extent associated with the variation of K^F (resp. δ^F),
 618 explained previously. These results related to the variation of Z_I against δ^F are found to be in
 619 agreement with those in *Sebben et al. [2015]*.

620 The dimensionless mass of salt persisting in the aquifer (M_S) appears to be sensitive to all
 621 uncertain parameters, except α_L^F (Fig. 13e). The total SIs with respect α_L^M , K^F , e^F , δ^F are
 622 calculated to be 0.34, 0.41, 0.22 and 0.27, respectively. The MEs show that M_S decreases
 623 with δ^F and increases with K^F and α_L^M (Figs. 14g-i). The variation against δ^F and K^F is
 624 related to the behavior of the saltwater wedge when these parameters change (see above). The
 625 increase of α_L^M pushes the saltwater wedge landward [*Fahs et al., 2018*] and increases the
 626 area of the salted zone as well as the mass of salt persisting in the aquifer. The total flux of
 627 saltwater entering the aquifer (Q_S^{total}) is mainly affected by α_L^M , K^F (Fig. 13f). The total SIs
 628 of these parameters are calculated to be 0.43 and 0.42, respectively. The MEs (Figs. 14j and
 629 14k) show that Q_S^{total} increases with α_L^M and decreases with K^F . Indeed, Q_S^{total} is advective
 630 and dispersive saltwater flux at the sea boundary. The dispersive flux is proportional to α_L^M .
 631 This explains why Q_S^{total} increases with α_L^M . The increase of K^F corresponds to the decrease
 632 of the gravity number (see above). A lower gravity number indicates less significant effect of
 633 the buoyancy forces for which the saltwater velocity decreases and reduces the advective
 634 saltwater flux. Finally, it is worth noting that, for the NOF configuration, the SIs for α_L^F are
 635 more important than for the SHF configuration. α_L^F appears to be an important parameter,
 636 especially for L_{toe} and L_s . In general, physical consistency of the results for both SHF and

637 NOF configuration provides insight on the validity of our analysis based on the PCE as a
638 meta-model.

639 **5. Conclusion**

640 In this work, the DFN model is coupled with the VDF model to simulate SWI in FCAs. The
641 DFN-VDF model requires the discontinuous description of the fracture characteristics which
642 are usually uncertain. Thus, it is essential, for several practical and theoretical purposes, to
643 understand/quantify how the uncertainties associated with the imperfect knowledge of the
644 fracture characteristics can propagate through the model and introduce uncertainties into the
645 model outputs. Despite the high performance of computer codes for SWI models, run-time of
646 these codes is still high because of the high nonlinearity, dense grids required for fractures
647 and large space and time scales associated with studied domains. Thus the traditional
648 techniques for uncertainty analysis (i.e. Monte-Carlo simulations) cannot be easily applied in
649 this context, as they require a large number of simulations to achieve reliable results. To meet
650 the computational challenges of traditional techniques, we develop in this work a GSA based
651 on the non-intrusive PCE. In particular, we apply an efficient sparse technique to construct the
652 PCE with a reduced number of model evaluations, based on Kashyap information criterion. In
653 the literature, GSA has been recently applied to SWI but previous studies are limited to
654 homogeneous domain. Two configurations of the fractured Henry Problem, dealing with a
655 single horizontal fracture (SHF) and a network of orthogonal fractures (NOF), are considered
656 as conceptual models. The simulations required to construct the PCE are performed using a
657 finite element model developed in the framework of COMSOL software. Boussinesq
658 approximation is implemented to improve the computational efficiency of the COMSOL
659 model. From technical point of view, this work shows several novelties that are important for
660 the simulation of SWI. It shows the ability of COMSOL to accurately simulate SWI in simple
661 and fractured aquifers. It also proves that the dimension reduction of fractures in the frame of

662 the DFN model is a valid approach to simulate SWI in FCAs and confirms the validity of the
663 Boussinesq approximation in such a case. Regarding uncertainty analysis, this study presents
664 an efficient (low cost) methodology to understand uncertainty propagation into SWI models.
665 This methodology is generic and can be efficiently applied to real field investigations. In
666 hydrogeological applications, GSA is often applied to investigate uncertainty propagation
667 associated with hydrogeological parameters. This work shows that GSA is generic and can be
668 a valuable tool for different kinds of uncertainties. The GSA results showed that, for the SHF
669 configuration, the uncertainty associated with the fracture hydraulic conductivity and depth is
670 the first sources of uncertainty on the salinity distribution. The spatial distributions of the SIs
671 are given as maps. This represents an important feature of this study as these maps are not
672 only important for uncertainty analysis but also provide relevant locations for measurement
673 required for aquifer characterization. Fracture hydraulic conductivity and depth are also
674 important parameters for the toe position (L_{toe}), thickness of the freshwater discharge zone
675 (Z_f), the mass of salt persisting in the aquifer (M_s) and the flux of saltwater entering the
676 aquifer (Q_s^{total}). The thickness of the saltwater wedge and the width of the mixing zone are
677 mainly controlled by the dispersion coefficient in the matrix. The uncertainty related to the
678 fracture aperture has a slight impact on the SWI metrics. Its major effect is observed on L_{toe} .
679 Uncertainty associated with the fracture dispersion coefficient does not affect in any way the
680 SWI metrics. For the NOF configuration, the imperfect knowledge of fracture hydraulic
681 conductivity and density are the first source of uncertainty of the salinity distribution.
682 However, it is observed that all the uncertain parameters become important for the salinity
683 distribution, in this case. In contrast to the SHF configuration, in which the dispersion in the
684 fracture is not important, in the NOF configuration the salinity distribution at the aquifer top
685 surface is influenced by this fracture dispersivity. L_{toe} and Z_f are mainly controlled by the

686 fractures density and hydraulic conductivity. As for the SHF configuration, the width of the
687 mixing zone is mainly affected by uncertainty associated with the dispersion coefficient in the
688 matrix. L_S is also majorly affected by the dispersion coefficient in the matrix, but the other
689 uncertain parameters are also influencing it. All the uncertain parameters have distributed
690 effects on M_S and Q_S^{total} .

691 **Acknowledgment**

692 Behzad Ataie-Ashtiani and Craig T. Simmons acknowledge support from the National Centre
693 for Groundwater Research and Training, Australia. Behzad Ataie-Ashtiani also appreciates
694 the support of the Research Office of the Sharif University of Technology, Iran. The authors
695 are grateful for Behzad Mozafari from Sharif University of Technology for useful discussion
696 on model development.

697

698

699

700

701

702

703

704

705

706

707

708

709

710 **References**

- 711 1. Arfib, B., Charlier, J.-B., 2016. Insights into saline intrusion and freshwater resources
712 in coastal karstic aquifers using a lumped Rainfall–Discharge–Salinity model (the
713 Port-Miou brackish spring, SE France). *Journal of Hydrology* 540, 148–161.
714 <https://doi.org/10.1016/j.jhydrol.2016.06.010>
- 715 2. Ataie-Ashtiani, B., Werner, A.D., Simmons, C.T., Morgan, L.K., Lu, C., 2013. How
716 important is the impact of land-surface inundation on seawater intrusion caused by
717 sea-level rise? *Hydrogeology Journal* 21, 1673–1677. <https://doi.org/10.1007/s10040-013-1021-0>
- 718 3. Bakalowicz, M., El Hakim, M., El-Hajj, A., 2008. Karst groundwater resources in the
719 countries of eastern Mediterranean: the example of Lebanon. *Environmental Geology*
720 54, 597–604. <https://doi.org/10.1007/s00254-007-0854-z>
- 721 4. Barragán, J.M., de Andrés, M., 2015. Analysis and trends of the world’s coastal cities
722 and agglomerations. *Ocean & Coastal Management* 114, 11–20.
723 <https://doi.org/10.1016/j.ocecoaman.2015.06.004>
- 724 5. Blatman, G., Sudret, B., 2011. Adaptive sparse polynomial chaos expansion based on
725 least angle regression. *Journal of Computational Physics* 230, 2345–2367.
726 <https://doi.org/10.1016/j.jcp.2010.12.021>
- 727 6. Bear, J., Cheng, A.H.-D., Sorek, S., Ouazar, D., Herrera, I. (Eds.), 1999. *Seawater
728 Intrusion in Coastal Aquifers: Concepts, Methods and Practices, Theory and
729 Applications of Transport in Porous Media*. Springer Netherlands.
- 730 7. Beaujean, J., Nguyen, F., Kemna, A., Antonsson, A., Engesgaard, P., 2014.
731 Calibration of seawater intrusion models: Inverse parameter estimation using surface
732 electrical resistivity tomography and borehole data. *Water Resources Research* 50,
733 6828–6849. <https://doi.org/10.1002/2013WR014020>
- 734 8. Berre, I., Doster, F., Keilegavlen, E., 2018. Flow in Fractured Porous Media: A
735 Review of Conceptual Models and Discretization Approaches. *Transport in Porous
736 Media*. <https://doi.org/10.1007/s11242-018-1171-6>
- 737 9. Chen, Z., Auler, A.S., Bakalowicz, M., Drew, D., Griger, F., Hartmann, J., Jiang, G.,
738 Moosdorf, N., Richts, A., Stevanovic, Z., Veni, G., Goldscheider, N., 2017. The
739 World Karst Aquifer Mapping project: concept, mapping procedure and map of
740 Europe. *Hydrogeology Journal* 25, 771–785. <https://doi.org/10.1007/s10040-016-1519-3>
- 741 10. Ciriello, V., Federico, V.D., Riva, M., Cadini, F., Sanctis, J.D., Zio, E., Guadagnini,
742 A., 2013. Polynomial chaos expansion for global sensitivity analysis applied to a
743 model of radionuclide migration in a randomly heterogeneous aquifer. *Stochastic
744 Environmental Research and Risk Assessment* 27, 945–954.
745 <https://doi.org/10.1007/s00477-012-0616-7>
- 746 11. Comte, J.-C., Offerdinger, U., Legchenko, A., Caulfield, J., Cassidy, R., González,
747 J.A.M., 2018. Catchment-scale heterogeneity of flow and storage properties in a
748 weathered/fractured hard rock aquifer from resistivity and magnetic resonance
749 surveys: implications for groundwater flow paths and the distribution of residence
750 times. *Geological Society, London, Special Publications* 479, SP479.11.
751 <https://doi.org/10.1144/SP479.11>
- 752 12. Crestaux, T., Le Maître, O., Martinez, J.-M., 2009. Polynomial chaos expansion for
753 sensitivity analysis. *Reliability Engineering & System Safety* 94, 1161–1172.
754 <https://doi.org/10.1016/j.res.2008.10.008>
- 755 13. Dai, H., Chen, X., Ye, M., Song, X., Zachara, J.M., 2017. A geostatistics-informed
756 hierarchical sensitivity analysis method for complex groundwater flow and transport
757 modeling. *Water Resources Research* 53, 4327–4343.
758
759

- 760 <https://doi.org/10.1002/2016WR019756>
- 761 14. De Rocquigny, E., 2012. *Modelling Under Risk and Uncertainty: An Introduction to*
762 *Statistical, Phenomenological and Computational Methods*. John Wiley & Sons.
- 763 15. Dell’Oca, A., Riva, M., Guadagnini, A., 2017. Moment-based metrics for global
764 sensitivity analysis of hydrological systems. *Hydrology and Earth System Sciences* 21,
765 6219–6234. <https://doi.org/10.5194/hess-21-6219-2017>
- 766 16. Deman, G., Konakli, K., Sudret, B., Kerrou, J., Perrochet, P., Benabderrahmane, H.,
767 2016. Using sparse polynomial chaos expansions for the global sensitivity analysis of
768 groundwater lifetime expectancy in a multi-layered hydrogeological model. *Reliability*
769 *Engineering & System Safety* 147, 156–169.
770 <https://doi.org/10.1016/j.res.2015.11.005>
- 771 17. Deng, B., Wang, J., 2017. Saturated-unsaturated groundwater modeling using 3D
772 Richards equation with a coordinate transform of nonorthogonal grids. *Applied*
773 *Mathematical Modelling* 50, 39–52. <https://doi.org/10.1016/j.apm.2017.05.021>
- 774 18. Dietrich, P., Helmig, R., Sauter, M., Hötzl, H., Köngeter, J., Teutsch, G. (Eds.), 2005.
775 *Flow and Transport in Fractured Porous Media*. Springer-Verlag, Berlin Heidelberg.
- 776 19. Dokou, Z., Karatzas, G.P., 2012. Saltwater intrusion estimation in a karstified coastal
777 system using density-dependent modelling and comparison with the sharp-interface
778 approach. *Hydrological Sciences Journal* 57, 985–999.
779 <https://doi.org/10.1080/02626667.2012.690070>
- 780 20. Fahs, H., Hayek, M., Fahs, M., Younes, A., 2014. An efficient numerical model for
781 hydrodynamic parameterization in 2D fractured dual-porosity media. *Advances in*
782 *Water Resources* 63, 179–193. <https://doi.org/10.1016/j.advwatres.2013.11.008>
- 783 21. Fahs, M., Ataie-Ashtiani, B., Younes, A., Simmons, C.T., Ackerer, P., 2016. The
784 Henry problem: New semianalytical solution for velocity-dependent dispersion. *Water*
785 *Resources Research* 52, 7382–7407. <https://doi.org/10.1002/2016WR019288>
- 786 22. Fahs, M., Koohbor, B., Belfort, B., Ataie-Ashtiani, B., Simmons, C., Younes, A.,
787 Ackerer, P., 2018. A Generalized Semi-Analytical Solution for the Dispersive Henry
788 Problem: Effect of Stratification and Anisotropy on Seawater Intrusion. *Water* 10,
789 230. <https://doi.org/10.3390/w10020230>
- 790 23. Fajraoui, N., Fahs, M., Younes, A., Sudret, B., 2017. Analyzing natural convection in
791 porous enclosure with polynomial chaos expansions: Effect of thermal dispersion,
792 anisotropic permeability and heterogeneity. *International Journal of Heat and Mass*
793 *Transfer* 115, 205–224. <https://doi.org/10.1016/j.ijheatmasstransfer.2017.07.003>
- 794 24. Fajraoui, N., Mara, T.A., Younes, A., Bouhlila, R., 2012. Reactive Transport
795 Parameter Estimation and Global Sensitivity Analysis Using Sparse Polynomial Chaos
796 Expansion. *Water, Air, & Soil Pollution* 223, 4183–4197.
797 <https://doi.org/10.1007/s11270-012-1183-8>
- 798 25. Fajraoui, N., Ramasomanana, F., Younes, A., Mara, T.A., Ackerer, P., Guadagnini,
799 A., 2011. Use of global sensitivity analysis and polynomial chaos expansion for
800 interpretation of nonreactive transport experiments in laboratory-scale porous media.
801 *Water Resources Research* 47. <https://doi.org/10.1029/2010WR009639>
- 802 26. Fidelibus, M.D., Calò, G., Tinelli, R., Tulipano, L., 2011. Salt ground waters in the
803 Salento karstic coastal aquifer (Apulia, Southern Italy), in: *Advances in the Research*
804 *of Aquatic Environment, Environmental Earth Sciences*. Springer, Berlin, Heidelberg,
805 pp. 407–415. https://doi.org/10.1007/978-3-642-19902-8_48
- 806 27. Fischer, P., Jardani, A., Cardiff, M., Lecoq, N., Jourde, H., 2018. Hydraulic analysis
807 of harmonic pumping tests in frequency and time domains for identifying the conduits
808 networks in a karstic aquifer. *Journal of Hydrology* 559, 1039–1053.
809 <https://doi.org/10.1016/j.jhydrol.2018.03.010>

- 810 28. Grillo, A., Logashenko, D., Stichel, S., Wittum, G., 2010. Simulation of density-
811 driven flow in fractured porous media. *Advances in Water Resources* 33, 1494–1507.
812 <https://doi.org/10.1016/j.advwatres.2010.08.004>
- 813 29. Guevara Morel, C.R., van Reeuwijk, M., Graf, T., 2015. Systematic investigation of
814 non-Boussinesq effects in variable-density groundwater flow simulations. *Journal of*
815 *Contaminant Hydrology* 183, 82–98. <https://doi.org/10.1016/j.jconhyd.2015.10.004>
- 816 30. Herckenrath, D., Langevin, C.D., Doherty, J., 2011. Predictive uncertainty analysis of
817 a saltwater intrusion model using null-space Monte Carlo. *Water Resources Research*
818 47. <https://doi.org/10.1029/2010WR009342>
- 819 31. Hirthe, E.M., Graf, T., 2015. Fracture network optimization for simulating 2D
820 variable-density flow and transport. *Advances in Water Resources* 83, 364–375.
821 <https://doi.org/10.1016/j.advwatres.2015.07.001>
- 822 32. Homma, T., Saltelli, A., 1996. Importance measures in global sensitivity analysis of
823 nonlinear models. *Reliability Engineering & System Safety* 52, 1–17.
824 [https://doi.org/10.1016/0951-8320\(96\)00002-6](https://doi.org/10.1016/0951-8320(96)00002-6)
- 825 33. Hu, C., Youn, B.D., 2011. Adaptive-sparse polynomial chaos expansion for reliability
826 and design of complex engineering systems. *Structural and Multidisciplinary*
827 *Optimization* 43, 419–442. <https://doi.org/10.1007/s00158-010-0568-9>
- 828 34. IOC/UNESCO, IMO, FAO, UNDP., 2011. A Blueprint for Ocean and Coastal
829 Sustainability, IOC/UNESCO. Paris.
- 830 35. Iooss, B., Lemaître, P., 2015. A Review on Global Sensitivity Analysis Methods, in:
831 Dellino, G., Meloni, C. (Eds.), *Uncertainty Management in Simulation-Optimization*
832 *of Complex Systems*. Springer US, Boston, MA, pp. 101–122.
833 https://doi.org/10.1007/978-1-4899-7547-8_5
- 834 36. Jerbi, C., Fournon, A., Noetinger, B., Delay, F., 2017. A new estimation of equivalent
835 matrix block sizes in fractured media with two-phase flow applications in dual
836 porosity models. *Journal of Hydrology* 548, 508–523.
837 <https://doi.org/10.1016/j.jhydrol.2017.03.028>
- 838 37. Jia, W., McPherson, B.J., Pan, F., Xiao, T., Bromhal, G., 2016. Probabilistic analysis
839 of CO₂ storage mechanisms in a CO₂-EOR field using polynomial chaos expansion.
840 *International Journal of Greenhouse Gas Control* 51, 218–229.
841 <https://doi.org/10.1016/j.ijggc.2016.05.024>
- 842 38. Kerrou, J., Renard, P., 2010. A numerical analysis of dimensionality and heterogeneity
843 effects on advective dispersive seawater intrusion processes. *Hydrogeology Journal*
844 18, 55–72. <https://doi.org/10.1007/s10040-009-0533-0>
- 845 39. Ketabchi, H., Mahmoodzadeh, D., Ataie-Ashtiani, B., Simmons, C.T., 2016. Sea-level
846 rise impacts on seawater intrusion in coastal aquifers: Review and integration. *Journal*
847 *of Hydrology* 535, 235–255. <https://doi.org/10.1016/j.jhydrol.2016.01.083>
- 848 40. Konakli, K., Sudret, B., 2016. Global sensitivity analysis using low-rank tensor
849 approximations. *Reliability Engineering & System Safety* 156, 64–83.
850 <https://doi.org/10.1016/j.ress.2016.07.012>
- 851 41. Le Gratiet, L., Marelli, S., Sudret, B., 2017. Metamodel-Based Sensitivity Analysis:
852 Polynomial Chaos Expansions and Gaussian Processes, in: Ghanem, R., Higdon, D.,
853 Owhadi, H. (Eds.), *Handbook of Uncertainty Quantification*. Springer International
854 Publishing, Cham, pp. 1289–1325. https://doi.org/10.1007/978-3-319-12385-1_38
- 855 42. Llopis-Albert, C., Merigó, J.M., Xu, Y., 2016. A coupled stochastic inverse/sharp
856 interface seawater intrusion approach for coastal aquifers under groundwater
857 parameter uncertainty. *Journal of Hydrology* 540, 774–783.
858 <https://doi.org/10.1016/j.jhydrol.2016.06.065>
- 859 43. Lu, C., Chen, Y., Zhang, C., Luo, J., 2013. Steady-state freshwater–seawater mixing

- 860 zone in stratified coastal aquifers. *Journal of Hydrology* 505, 24–34.
861 <https://doi.org/10.1016/j.jhydrol.2013.09.017>
- 862 44. MacAllister, D., Jackson, M.D., Butler, A.P., Vinogradov, J., 2018. Remote Detection
863 of Saline Intrusion in a Coastal Aquifer Using Borehole Measurements of Self-
864 Potential. *Water Resources Research* 54, 1669–1687.
865 <https://doi.org/10.1002/2017WR021034>
- 866 45. Maina, F.Z., Guadagnini, A., 2018. Uncertainty Quantification and Global Sensitivity
867 Analysis of Subsurface Flow Parameters to Gravimetric Variations During Pumping
868 Tests in Unconfined Aquifers. *Water Resources Research* 54, 501–518.
869 <https://doi.org/10.1002/2017WR021655>
- 870 46. Marelli, S., Sudret, B., 2014. UQLab: A Framework for Uncertainty Quantification in
871 Matlab. *American Society of Civil Engineers*, pp. 2554–2563.
872 <https://doi.org/10.1061/9780784413609.257>
- 873 47. Mehdizadeh, S.S., Werner, A.D., Vafaie, F., Badaruddin, S., 2014. Vertical leakage in
874 sharp-interface seawater intrusion models of layered coastal aquifers. *Journal of*
875 *Hydrology* 519, 1097–1107. <https://doi.org/10.1016/j.jhydrol.2014.08.027>
- 876 48. Meng, J., Li, H., 2017. Efficient Uncertainty Quantification for Unconfined Flow in
877 Heterogeneous Media with the Sparse Polynomial Chaos Expansion. *Transport in*
878 *Porous Media*. <https://doi.org/10.1007/s11242-017-0974-1>
- 879 49. Miller, K.L., Berg, S.J., Davison, J.H., Sudicky, E.A., Forsyth, P.A., 2018. Efficient
880 uncertainty quantification in fully-integrated surface and subsurface hydrologic
881 simulations. *Advances in Water Resources* 111, 381–394.
882 <https://doi.org/10.1016/j.advwatres.2017.10.023>
- 883 50. Mozafari, B., Fahs, M., Ataie-Ashtiani, B., Simmons, C.T., Younes, R., 2018. On the
884 use of COMSOL Multiphysics for seawater intrusion in fractured coastal aquifers.
885 *E3S Web of Conferences* 54, 00020. <https://doi.org/10.1051/e3sconf/20185400020>
- 886 51. Perriquet, M., Leonardi, V., Henry, T., Jourde, H., 2014. Saltwater wedge variation in
887 a non-anthropogenic coastal karst aquifer influenced by a strong tidal range (Burren,
888 Ireland). *Journal of Hydrology* 519, 2350–2365.
889 <https://doi.org/10.1016/j.jhydrol.2014.10.006>
- 890 52. Pool, M., Post, V.E.A., Simmons, C.T., 2015. Effects of tidal fluctuations and spatial
891 heterogeneity on mixing and spreading in spatially heterogeneous coastal aquifers.
892 *Water Resources Research* 51, 1570–1585. <https://doi.org/10.1002/2014WR016068>
- 893 53. Rajabi, M.M., Ataie-Ashtiani, B., 2014. Sampling efficiency in Monte Carlo based
894 uncertainty propagation strategies: Application in seawater intrusion simulations.
895 *Advances in Water Resources* 67, 46–64.
896 <https://doi.org/10.1016/j.advwatres.2014.02.004>
- 897 54. Rajabi, M.M., Ataie-Ashtiani, B., Simmons, C.T., 2015. Polynomial chaos expansions
898 for uncertainty propagation and moment independent sensitivity analysis of seawater
899 intrusion simulations. *Journal of Hydrology* 520, 101–122.
900 <https://doi.org/10.1016/j.jhydrol.2014.11.020>
- 901 55. Ramasomanana, F., Fahs, M., Baalousha, H.M., Barth, N., Ahzi, S., 2018. An
902 Efficient ELLAM Implementation for Modeling Solute Transport in Fractured Porous
903 Media. *Water, Air, & Soil Pollution* 229, 46. <https://doi.org/10.1007/s11270-018-3690-8>
- 904 56. Ren, F., Ma, G., Wang, Y., Li, T., Zhu, H., 2017. Unified pipe network method for
905 simulation of water flow in fractured porous rock. *Journal of Hydrology* 547, 80–96.
906 <https://doi.org/10.1016/j.jhydrol.2017.01.044>
- 907 57. Riva, M., Guadagnini, A., Dell’Oca, A., 2015. Probabilistic assessment of seawater
908 intrusion under multiple sources of uncertainty. *Advances in Water Resources* 75, 93–
909

- 910 104. <https://doi.org/10.1016/j.advwatres.2014.11.002>
- 911 58. Saltelli, A., 2002. Making best use of model evaluations to compute sensitivity
912 indices. *Computer Physics Communications* 145, 280–297.
913 [https://doi.org/10.1016/S0010-4655\(02\)00280-1](https://doi.org/10.1016/S0010-4655(02)00280-1)
- 914 59. Sarkar, S., Witteveen, J.A., 2016. *Uncertainty Quantification In Computational*
915 *Science: Theory And Application In Fluids And Structural Mechanics*. World
916 Scientific.
- 917 60. Saylor, C., Cardiff, M., Fort, M.D., 2018. Understanding the Geometry of Connected
918 Fracture Flow with Multiperiod Oscillatory Hydraulic Tests. *Groundwater* 56, 276–
919 287. <https://doi.org/10.1111/gwat.12580>
- 920 61. Sebben, M.L., Werner, A.D., Graf, T., 2015. Seawater intrusion in fractured coastal
921 aquifers: A preliminary numerical investigation using a fractured Henry problem.
922 *Advances in Water Resources* 85, 93–108.
923 <https://doi.org/10.1016/j.advwatres.2015.09.013>
- 924 62. Shao, Q., Younes, A., Fahs, M., Mara, T.A., 2017. Bayesian sparse polynomial chaos
925 expansion for global sensitivity analysis. *Computer Methods in Applied Mechanics*
926 *and Engineering* 318, 474–496. <https://doi.org/10.1016/j.cma.2017.01.033>
- 927 63. Shi, W., Lu, C., Ye, Y., Wu, J., Li, L., Luo, J., 2018. Assessment of the impact of sea-
928 level rise on steady-state seawater intrusion in a layered coastal aquifer. *Journal of*
929 *Hydrology* 563, 851–862. <https://doi.org/10.1016/j.jhydrol.2018.06.046>
- 930 64. Simmons, C.T., Fenstemaker, T.R., Sharp, J.M., 2001. Variable-density groundwater
931 flow and solute transport in heterogeneous porous media: approaches, resolutions and
932 future challenges. *Journal of Contaminant Hydrology* 52, 245–275.
933 [https://doi.org/10.1016/S0169-7722\(01\)00160-7](https://doi.org/10.1016/S0169-7722(01)00160-7)
- 934 65. Sobol', I.M., 2001. Global sensitivity indices for nonlinear mathematical models and
935 their Monte Carlo estimates. *Mathematics and Computers in Simulation, The Second*
936 *IMACS Seminar on Monte Carlo Methods* 55, 271–280.
937 [https://doi.org/10.1016/S0378-4754\(00\)00270-6](https://doi.org/10.1016/S0378-4754(00)00270-6)
- 938 66. Stoeckl, L., Houben, G.J., Dose, E.J., 2015. Experiments and modeling of flow
939 processes in freshwater lenses in layered island aquifers: Analysis of age stratification,
940 travel times and interface propagation. *Journal of Hydrology* 529, 159–168.
941 <https://doi.org/10.1016/j.jhydrol.2015.07.019>
- 942 67. Sudret, B., 2008. Global sensitivity analysis using polynomial chaos expansions.
943 *Reliability Engineering & System Safety* 93, 964–979.
944 <https://doi.org/10.1016/j.res.2007.04.002>
- 945 68. Szymkiewicz, A., Gumuła-Kawęcka, A., Šimůnek, J., Leterme, B., Beegum, S.,
946 Jaworska-Szulc, B., Pruszkowska-Caceres, M., Gorczewska-Langner, W., Angulo-
947 Jaramillo, R., Jacques, D., 2018. Simulations of freshwater lens recharge and
948 salt/freshwater interfaces using the HYDRUS and SWI2 packages for MODFLOW.
949 *Journal of Hydrology and Hydromechanics* 66, 246–256. <https://doi.org/10.2478/johh-2018-0005>
- 950
- 951 69. Werner, A.D., Bakker, M., Post, V.E.A., Vandenbohede, A., Lu, C., Ataie-Ashtiani,
952 B., Simmons, C.T., Barry, D.A., 2013. Seawater intrusion processes, investigation and
953 management: Recent advances and future challenges. *Advances in Water Resources*
954 51, 3–26. <https://doi.org/10.1016/j.advwatres.2012.03.004>
- 955 70. Xu, Z., Hu, B.X., Ye, M., 2018. Numerical modeling and sensitivity analysis of
956 seawater intrusion in a dual-permeability coastal karst aquifer with conduit networks.
957 *Hydrology and Earth System Sciences* 22, 221–239. <https://doi.org/10.5194/hess-22-221-2018>
- 958
- 959 71. Younes, A., Delay, F., Fajraoui, N., Fahs, M., Mara, T.A., 2016. Global sensitivity

- 960 analysis and Bayesian parameter inference for solute transport in porous media
961 colonized by biofilms. *Journal of Contaminant Hydrology* 191, 1–18.
962 <https://doi.org/10.1016/j.jconhyd.2016.04.007>
- 963 72. Younes, A., Mara, T.A., Fajraoui, N., Lehmann, F., Belfort, B., Beydoun, H., 2013.
964 Use of Global Sensitivity Analysis to Help Assess Unsaturated Soil Hydraulic
965 Parameters. *Vadose Zone Journal* 12, 0. <https://doi.org/10.2136/vzj2011.0150>
- 966 73. Younes, A., Zaouali, J., Lehmann, F., Fahs, M., 2018. Sensitivity and identifiability of
967 hydraulic and geophysical parameters from streaming potential signals in unsaturated
968 porous media. *Hydrology and Earth System Sciences* 22, 3561–3574.
969 <https://doi.org/10.5194/hess-22-3561-2018>
- 970 74. Younes, A., Fahs, M., Ahmed, S., 2009. Solving density driven flow problems with
971 efficient spatial discretizations and higher-order time integration methods. *Advances*
972 *in Water Resources* 32, 340–352. <https://doi.org/10.1016/j.advwatres.2008.11.003>

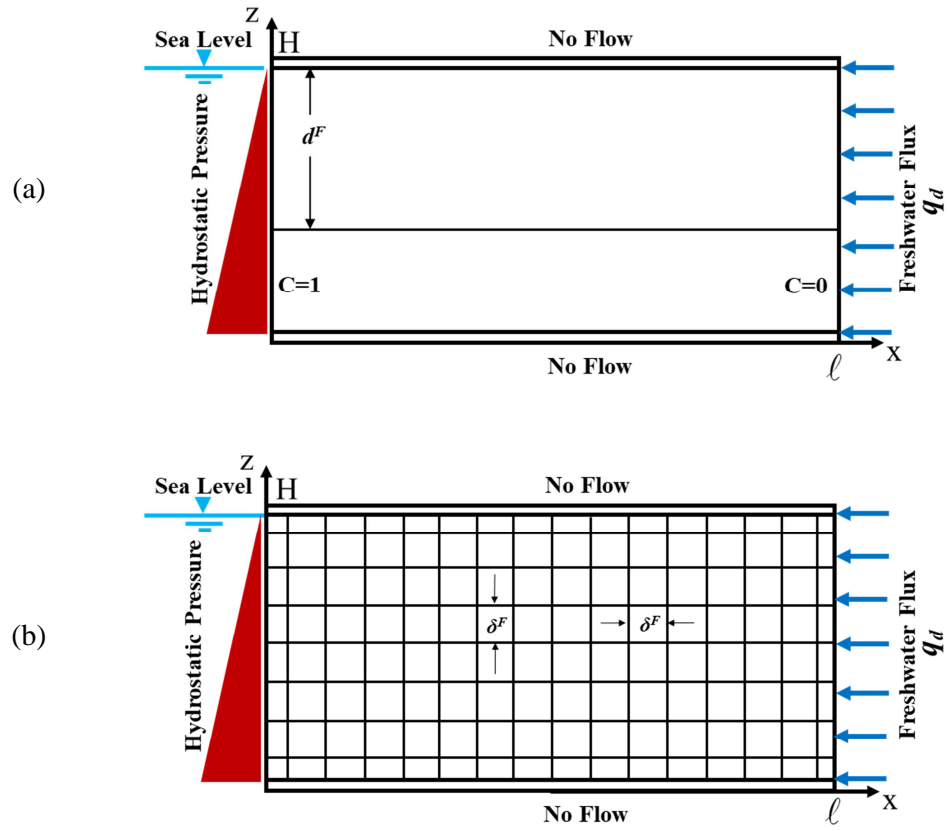


Fig. 1. Conceptual model of the fractured Henry Problem: (a) Single horizontal fracture configuration (SHF) and (b) Network of orthogonal fractures configuration (NOF).

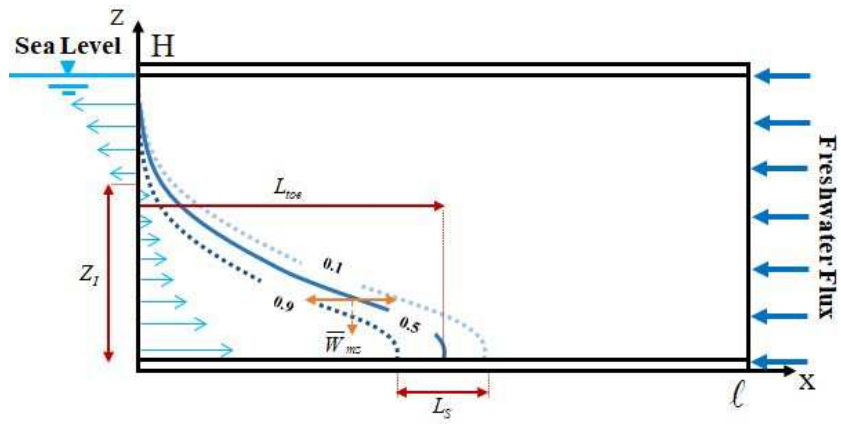


Fig. 2. Schematic representation of the SWI metrics.

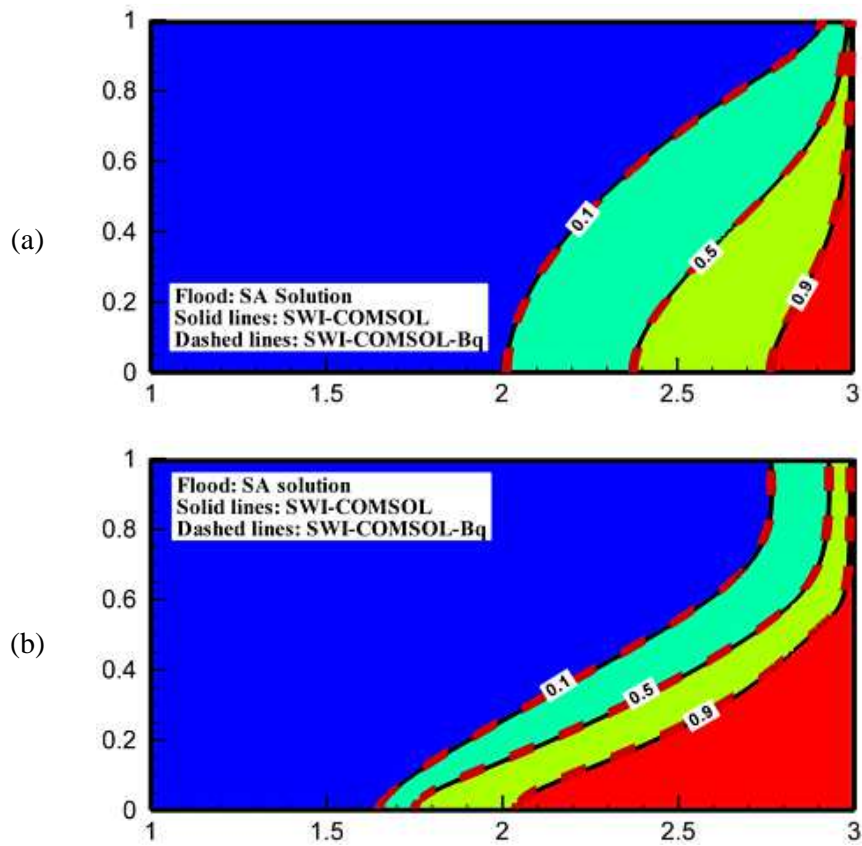


Fig. 3. Isochlors obtained using the semi-analytical solution (SA) and COMSOL model (with and without Boussinesq approximation) for the homogenous test cases: (a) diffusive case and (b) dispersive case.

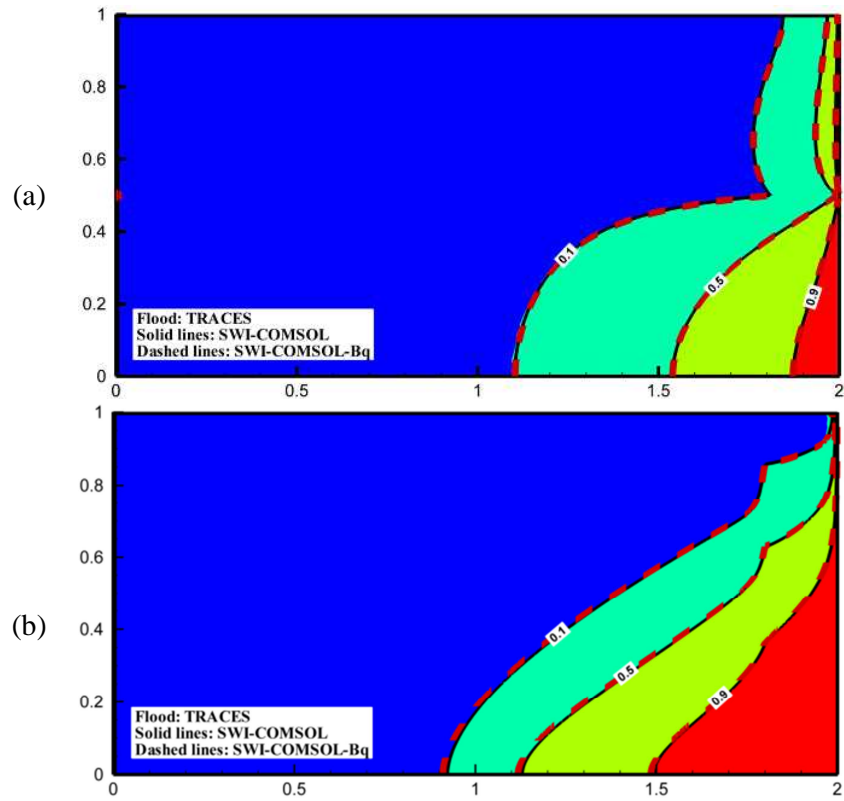


Fig. 4. Isochlors obtained using TRACES (in-house code) and COMSOL model (with and without Boussinesq approximation) for the fractured test cases: a) single horizontal fracture and b) single vertical fracture.

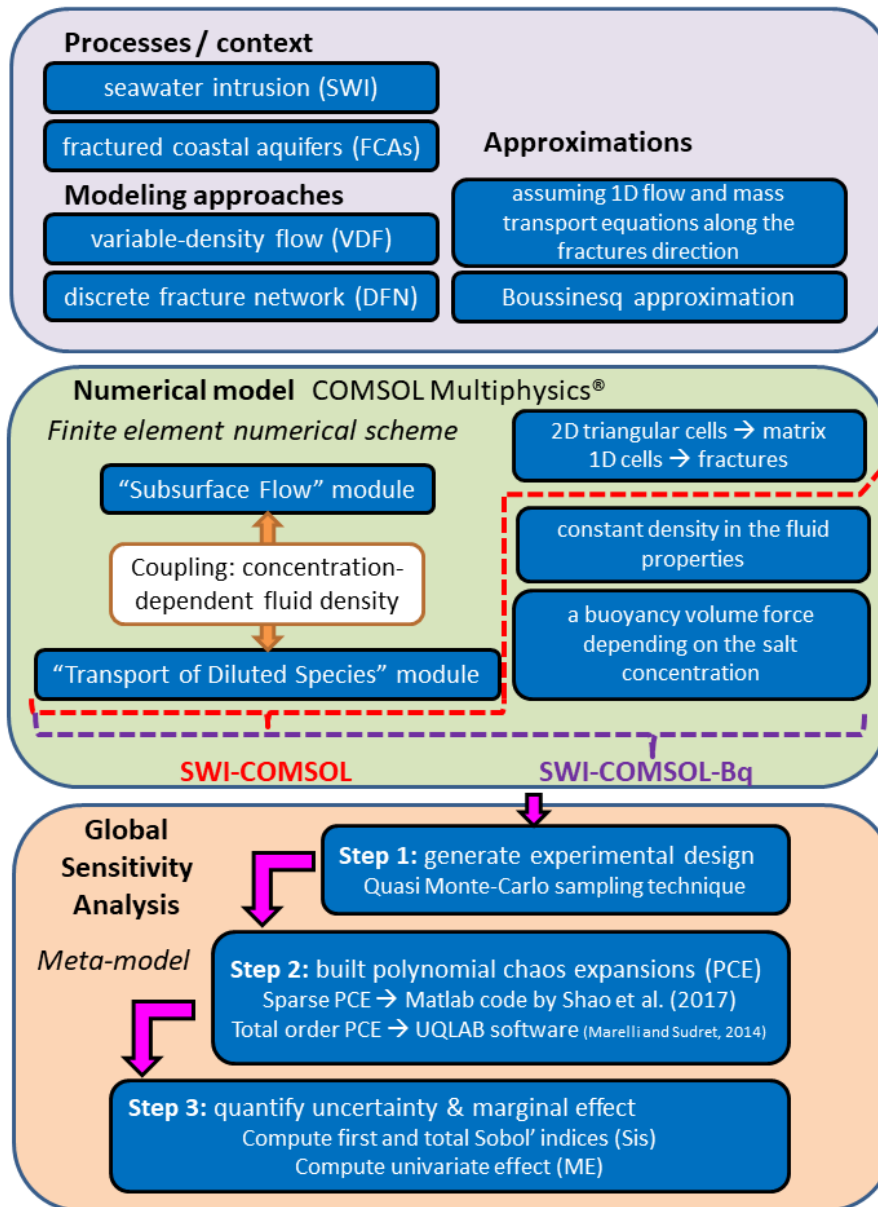
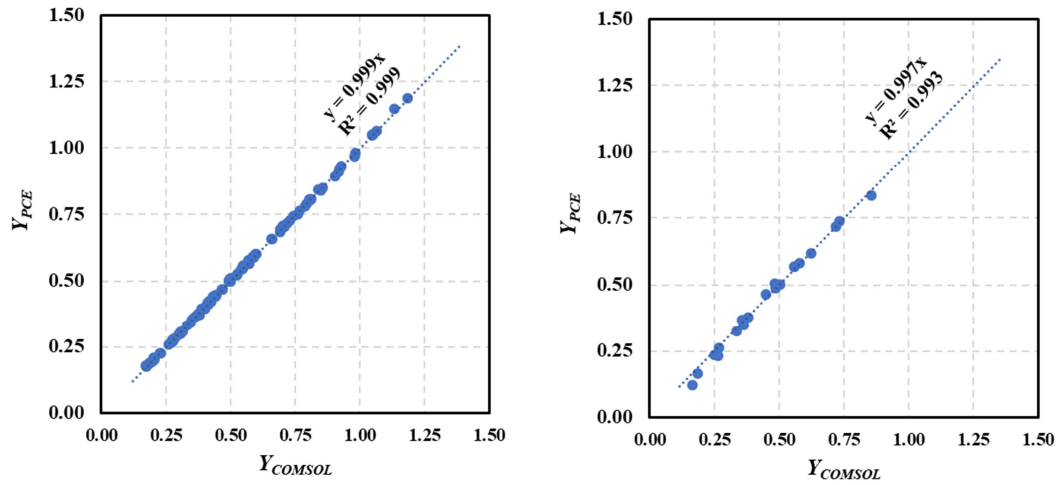
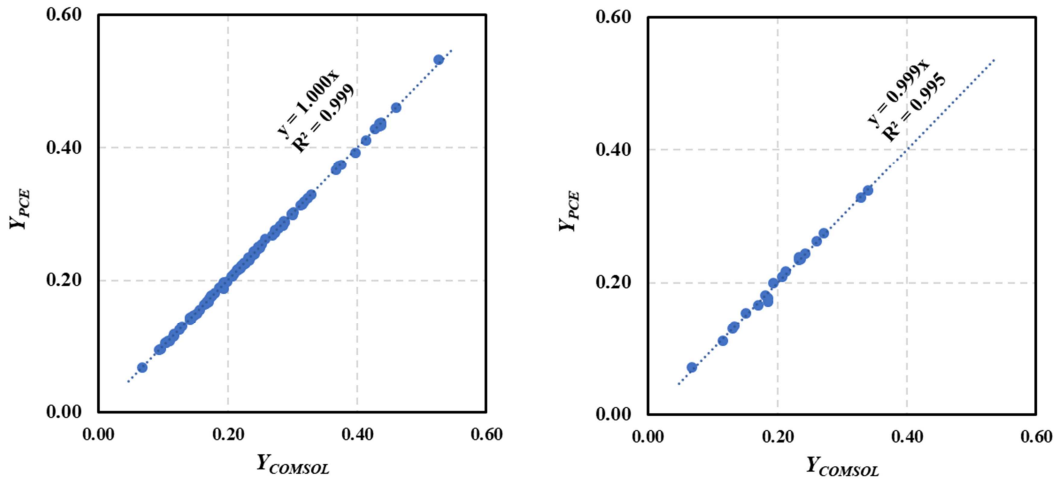


Fig. 5. A flowchart describing the methodology and approaches used to perform the global sensitivity analysis: The first block (in purple) describes the physical processes and the corresponding mathematical models used in this study; The second block (in olive-green) presents the finite element model used to simulate the physical processes (COMSOL with and without Boussinesq approximation); The third block (in orange) describes the approach used to perform global sensitivity analysis (polynomial chaos expansion as meta-model and Sobol's indices as sensitivity metrics).



a) The length of the saltwater toe (L_{toe}).



b) The dimensionless mass of salt persisting in the aquifer (M_s).

Fig. 6. Comparison between the PCE surrogate model and physical (COMSOL) model for the SHF configuration: On the left side, 100 samples used for the experimental design and on the right side, 20 simulations which do not coincide with the experimental design (R^2 is the coefficient of determination).

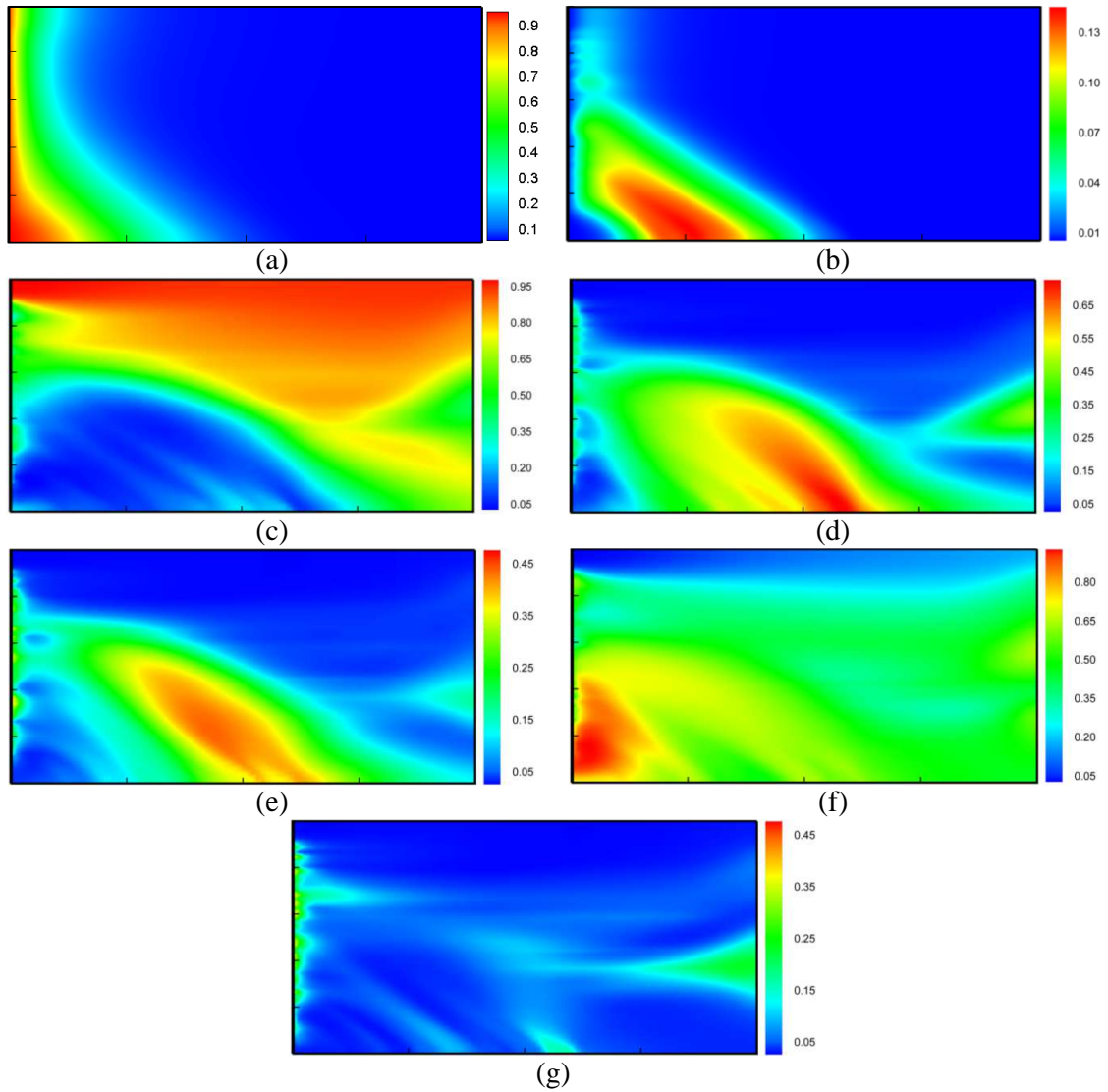


Fig. 7. GSA results for the spatial distribution of the salt concentration (SHF configuration): (a) mean salt concentration (b) variance of the salt concentration, (c) total SI of α_L^M , (d) total SI of K^F , (e) total SI of e^F , (f) total SI index of d^F and (g) total SI index of α_L^F .

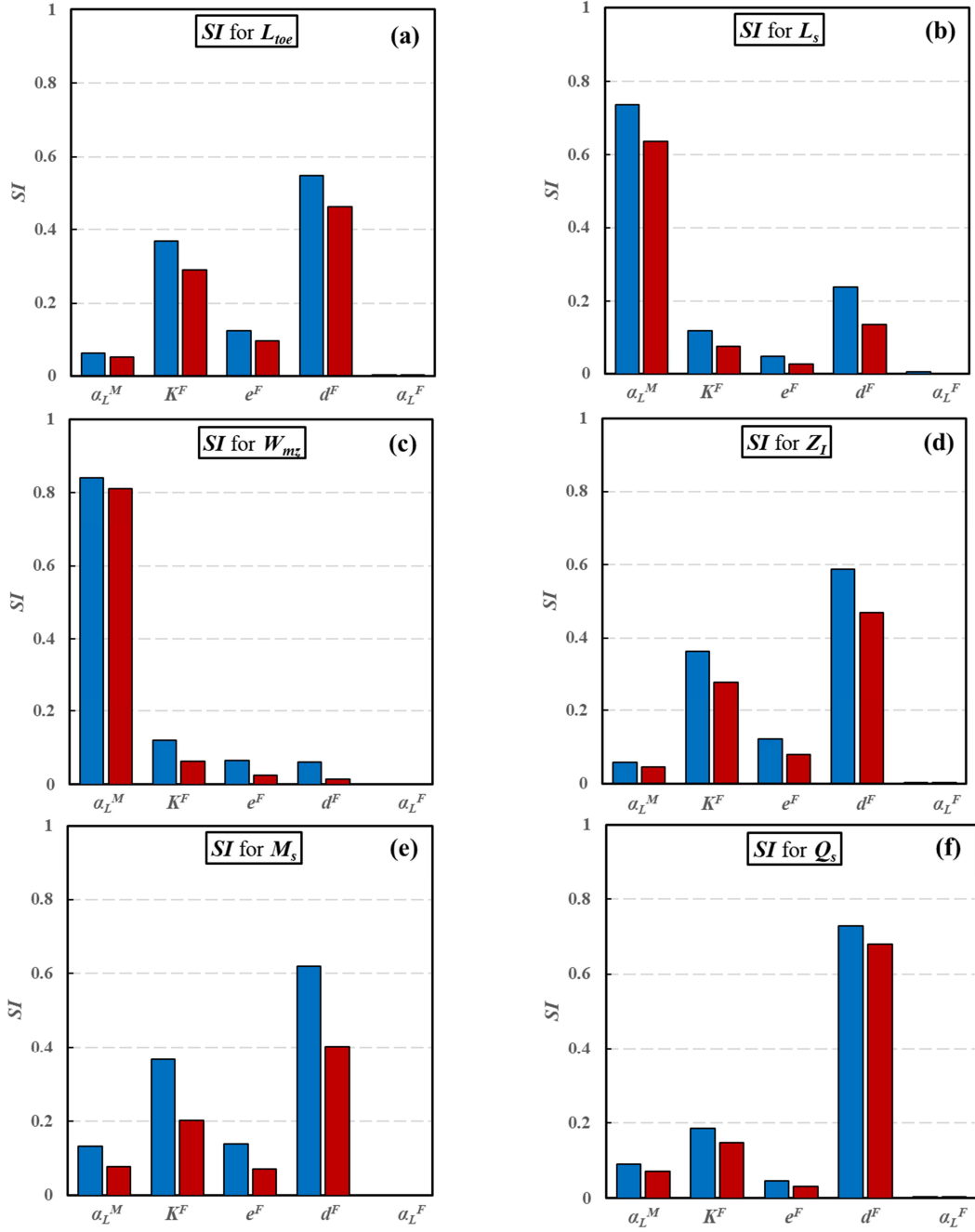


Fig. 8. Total (blue) and first order (red) SIs for the SHF configuration: (a) L_{toe} , (b) L_s , (c) \overline{W}_{mz} , (d) Z_I , (e) M_s and (f) Q_s^{total} .

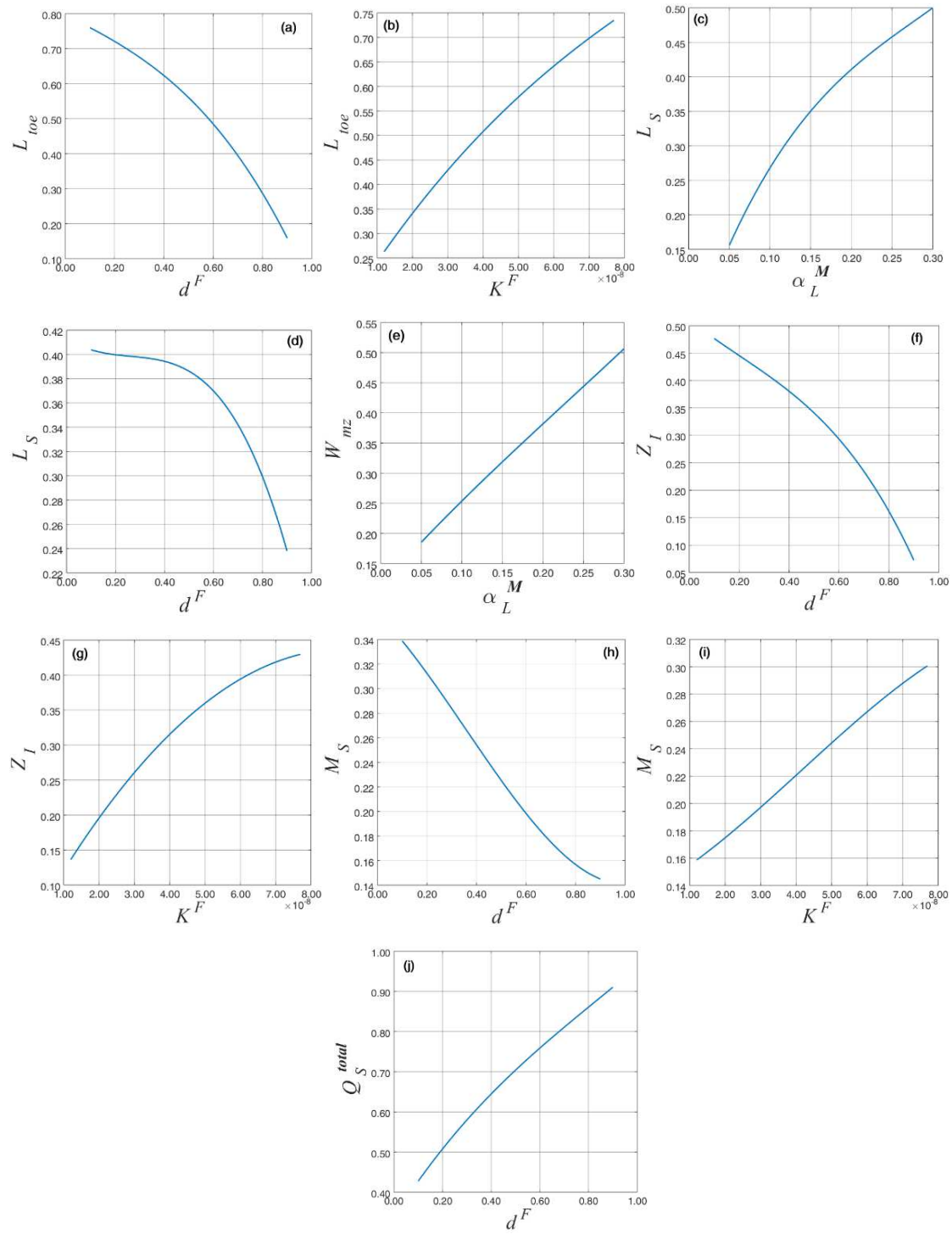
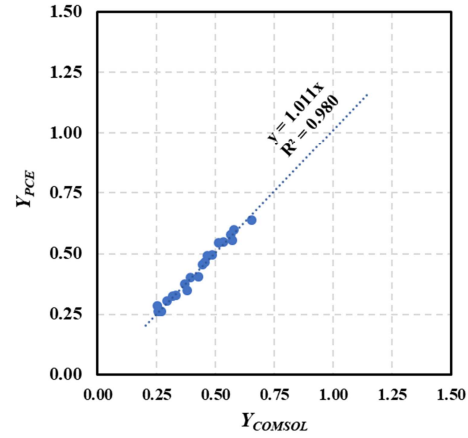
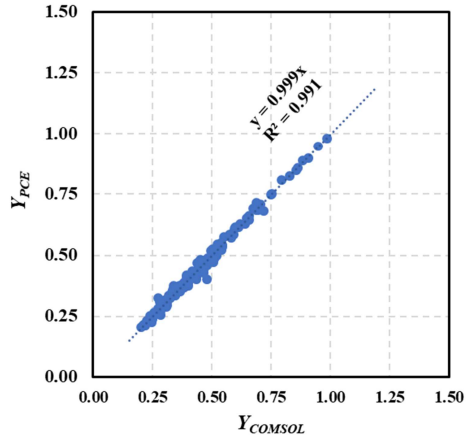
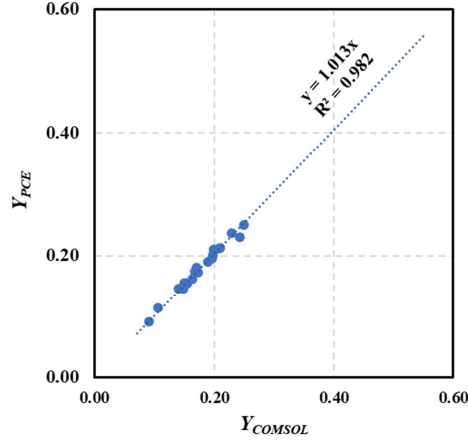
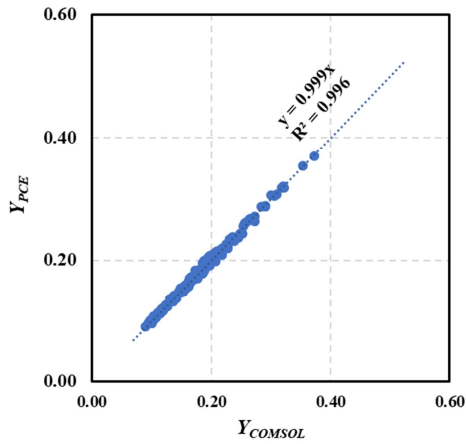


Fig. 9. The marginal effects of uncertain parameters on SWI metrics for the SHF configuration.



a) The length of the saltwater toe (L_{toe})



b) The dimensionless mass of salt persisting in the aquifer (M_s).

Fig. 10. Comparison between the PCE surrogate and physical (COMSOL) models for the NOF configuration: On the left side, 200 samples used for the experimental design and on the right side, 20 simulations which do not coincide with the experimental design.

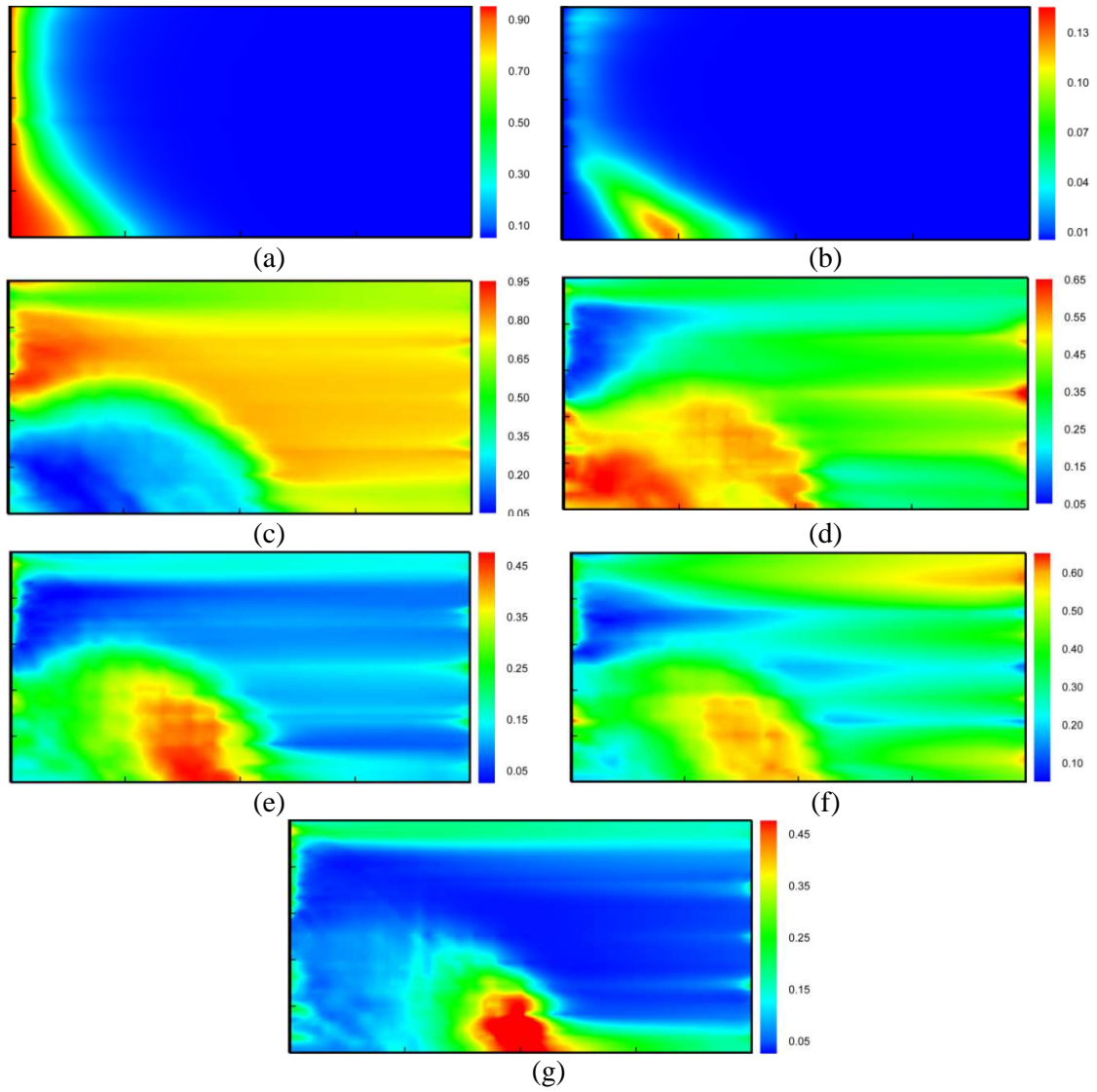


Fig. 11. GSA results for the spatial distribution of the salt concentration (NOF configuration):

- (a) mean salt concentration (b) variance of the salt concentration, (c) total SI of α_L^M , (d) total SI of K^F , (e) total SI of e^F , (f) total SI index of δ^F and (g) total SI index of α_L^F

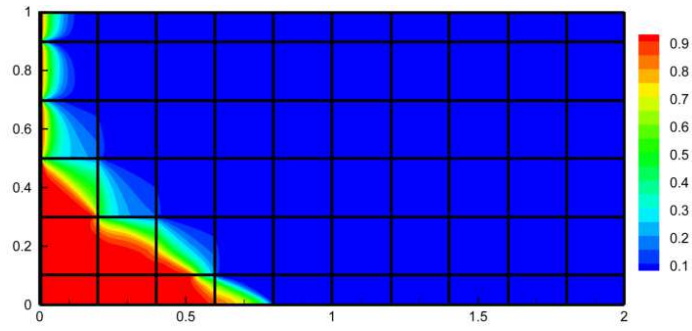


Fig. 12. Isochlors distribution for the NOF configuration ($\alpha_L^M = \alpha_L^F = 0.05m$; $K^F = 0.07m/s$; $e^F = 0.1mm$; $\delta^F = 0.2m$, others parameters are the same as Table 3).

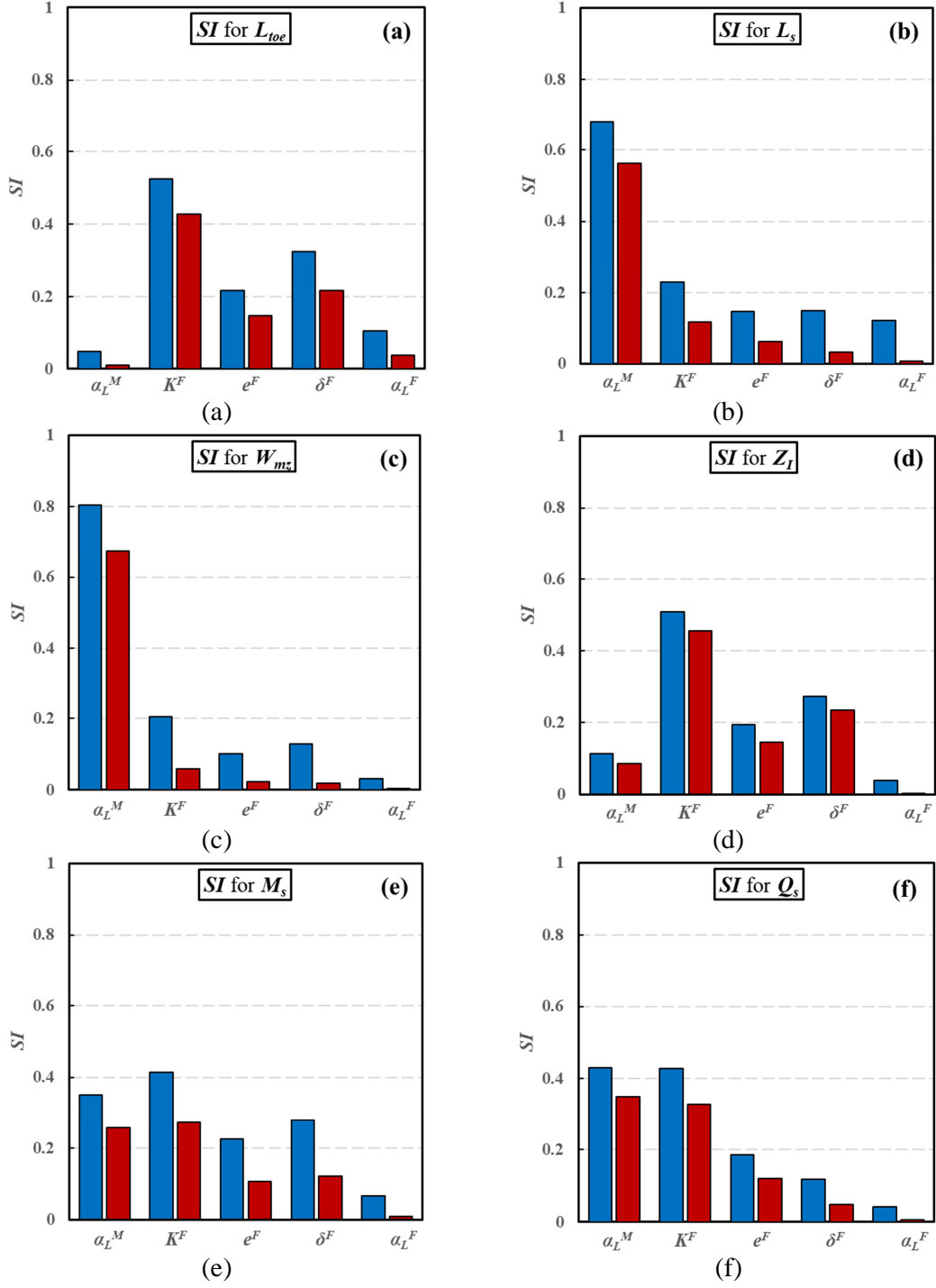


Fig. 13. Total (blue) and first order (red) SIs for the NOF configuration: (a) L_{tot} , (b) L_s , (c) \bar{W}_{mz} , (d) Z_I , (e) M_s and (f) Q_s^{total} .

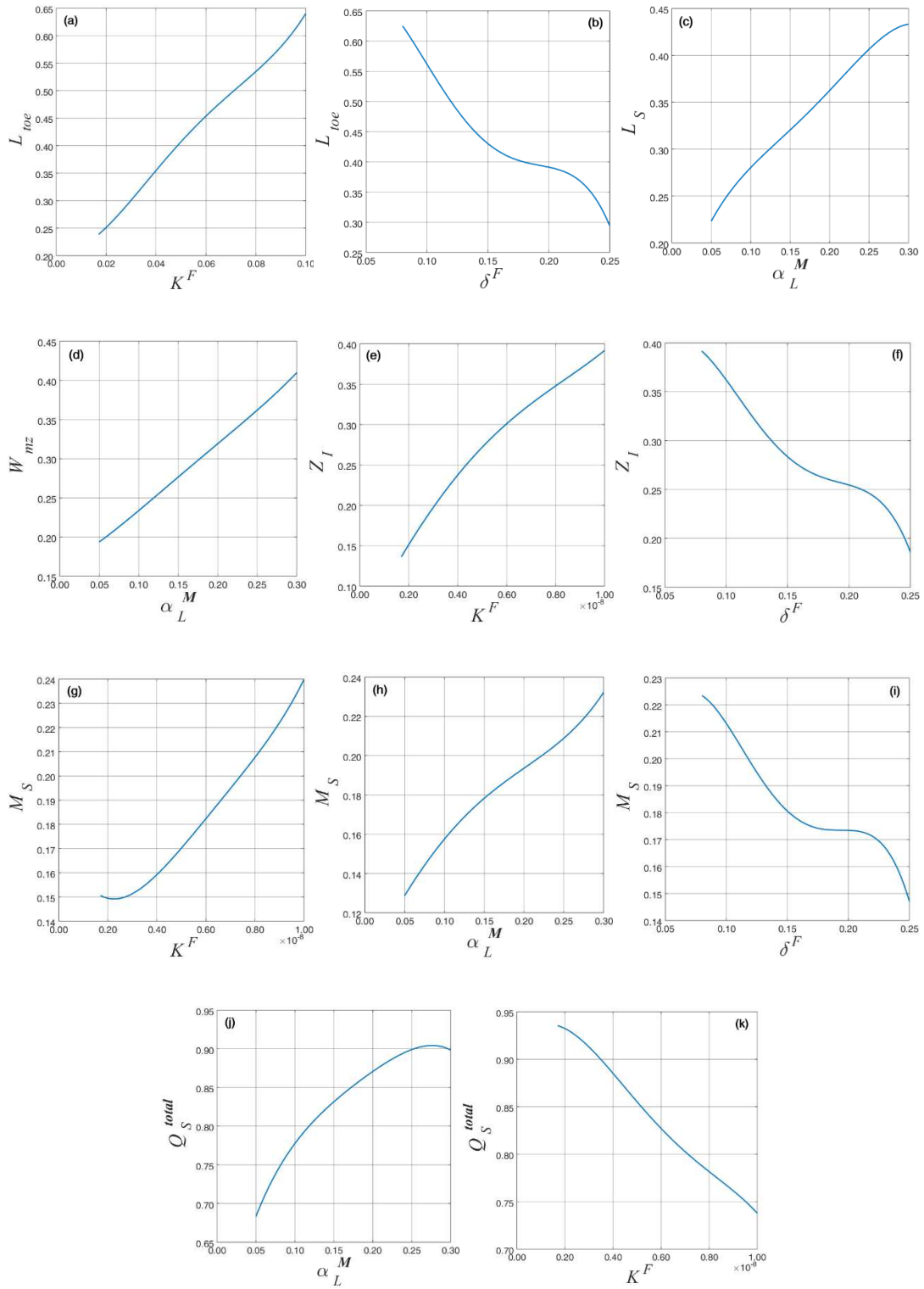


Fig. 14. The marginal effects of uncertain parameters on SWI metrics for the NOF configuration.

Table 1. Physical parameters used for the validation of homogeneous and fractured cases

Parameters	Homogenous cases		Fractured cases
$\rho_1 [kg/m^3]$	1,025		1,025
$\rho_0 [kg/m^3]$	1,000		1,000
$q_d [m^2/s]$	6.6×10^{-5}		6.6×10^{-6}
$H [m]$	1		1
$\ell [m]$	3		2
$K^M [m/s]$	1.001×10^{-2}		2.5×10^{-4} Horizontal Fracture 1.0×10^{-3} Vertical Fracture
$K^F [m/s]$	-		7.72×10^{-1}
$\varepsilon^M [-]$	0.35		0.2
$\varepsilon^F [-]$	-		1.0
$e^F [m]$	-		0.001
$d^F [m]$	-		0.5
$D_m [m^2/s]$	18.86×10^{-6} 9.43×10^{-8}	Diffusive case Dispersive case	18.86×10^{-7} Horizontal Fracture 1.0×10^{-6} Vertical Fracture
$\alpha_L^M [m]$	0	Diffusive case	0
	0.1	Dispersive case	
$\alpha_T^M [m]$	0	Diffusive case	0
	0.01	Dispersive case	
$\alpha_L^F [m]$	-		0
$\alpha_T^F [m]$	-		0

Table 2. SWI metrics for the validation cases: Semi-analytical solution (S-Anl), SWI-COMSOL (Co-st) and SWI-COMSOL-Bq (CO-Bq). The width of the mixing zone for the homogenous case is calculated vertically as in *Fahs et al. [2016]*.

Metrics	Homogenous Diffusive			Homogenous Dispersive			Fractured (Horizontal)		
	S-Anl	CO-St	CO-Bq	S-Anl	CO-St	CO-Bq	TRACES	CO-St	CO-Bq
L_{toe}	0.624	0.626	0.625	1.256	1.253	1.251	0.460	0.461	0.460
L_S	0.751	0.754	0.752	0.368	0.392	0.391	0.768	0.777	0.776
\overline{W}_{mz}	0.757	0.763	0.760	0.295	0.295	0.294	0.451	0.455	0.455
Z_I	0.419	0.430	0.429	0.527	0.521	0.519	0.492	0.478	0.478
M_S	0.109	0.109	0.109	0.150	0.151	0.150	0.113	0.114	0.114
Q_S^{total}	1.068	0.970	0.976	1.061	1.037	1.049	0.625	0.618	0.622

Table 3. Values and ranges of variability of the parameters used for the GSA.

Parameters	Configuration SHF	Configuration NOF
ρ_1 [kg/m^3]	1,025	1,025
ρ_0 [kg/m^3]	1,000	1,000
q_d [m^2/s]	6.6×10^{-6}	6.6×10^{-6}
H [m]	1	1
ℓ [m]	2	2
K^M [m/s]	2.49×10^{-5}	2.49×10^{-5}
K^F [m/s]	$[1.17 \times 10^{-1} - 7.65 \times 10^{-1}]$	$[1.86 \times 10^{-2} - 1.17 \times 10^{-1}]$
ε^M [-]	0.2	0.2
ε^F [-]	1.0	1.0
e^F [m]	$[3.8 \times 10^{-4} - 9.7 \times 10^{-4}]$	$[3.8 \times 10^{-4} - 9.7 \times 10^{-4}]$
d^F [m]	[0.1 – 0.9]	-
δ^F [m]	-	[0.08 – 0.25]
D_m [m^2/s]	10^{-9}	10^{-9}
α_L^M [m]	[0.05 – 0.3]	[0.05 – 0.3]
α_T^M [m]	$0.1 \times \alpha_L^M$	$0.1 \times \alpha_L^M$
α_L^F [m]	[0.05 – 0.3]	[0.05 – 0.3]
α_T^F [m]	0	0

